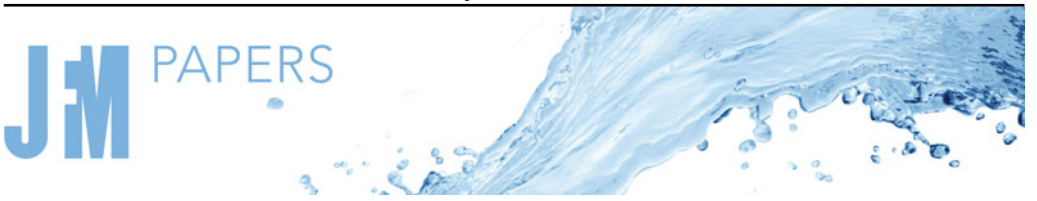
J. Fluid Mech. (2026), *vol.* 1038, A41, doi:10.1017/jfm.2026.11781



Cavitation bubble collapse near a wall: a numerical study on a bubble initially generated by laser

Bo Wang[1], **Zhidian Yang**[1], **Kevin Wang**[2], **Olivier Coutier-Delgosha**[1,2] and **Francesco Romanò**[1]

[1]Univ. Lille, CNRS, ONERA, Centrale Lille, Arts et Métiers Institute of Technology, UMR 9014 - LMFL - Laboratoire de Mécanique des Fluides de Lille - Kampé de Fériet, Lille F-59000, France

[2]Kevin T. Crofton Department of Aerospace and Ocean Engineering, Virginia Tech, Blacksburg, VA 24060, USA

Corresponding author: Bo Wang, bo.wang_1@ensam.eu

(Received 28 October 2025 UTC; revised 21 April 2026 UTC; accepted 4 June 2026 UTC)

Cavitation bubble collapse near a wall is investigated by employing a recently developed laser–fluid computational framework to simulate the complete lifecycle of a wall-detached laser-induced bubble, including the water breakdown phase. The model couples compressible multiphase Euler equations, a radiative transport equation and a latent heat reservoir formulation for phase transition. A wide range of nine stand-off ratios $\gamma \in [0.79,\ 2.14]$ is investigated and directly compared with recent experimental measurements. The simulations reproduce the interfacial dynamics of bubbles with excellent accuracy. Moreover, the computations are capable of reidentifying the three experimentally observed collapse regimes, i.e. purely torus, mixed tip-and-torus and purely tip collapse, and correctly identify the collapse as the dominant source of the peak wall pressure rather than jet impact. A sensitivity analysis shows that only the mixed tip-and-torus regime exhibits strong dependence on the laser absorption coefficient. The simulations give access to the details on pressure, density, temperature and velocity fields inside the bubble and demonstrate that the vapour remains in average thermodynamic equilibrium during most of lifetime. The results reveal significantly different time scales between thermodynamic fields where the gas pressure becomes quasi-uniform inside the bubble during expansion and collapse, whereas the temperature remains strongly non-uniform with persistent spatial gradients. This study provides the most complete numerical

© The Author(s), 2026. Published by Cambridge University Press. This is an Open Access article, distributed under the terms of the Creative Commons Attribution licence (https://creativecommons.org/licenses/by/4.0/), which permits unrestricted re-use, distribution and reproduction, provided the original article is properly cited.

https://doi.org/10.1017/jfm.2026.11781 Published online by Cambridge University Press

reproduction to date of experimental laser-induced bubble collapse near a wall, and offers new physical insight into the coupling between bubble–wall interaction, laser-induced thermodynamics and collapse regimes.

Key words: cavitation, bubble dynamics

1. Introduction

Cavitation bubbles commonly appear in hydraulic machinery such as pumps and turbines (Arndt 1981; Cristofaro *et al.* 2020; Balz *et al.* 2021). Their collapse near solid surfaces can produce extremely high local pressures, intense microjets and pressure waves, leading to severe mechanical and structural damage. Harrison (1952) provided one of the first experimental measurements of single bubble collapse, showing that shock pressures can reach tens of megapascals, sufficient to damage nearby metal surfaces. Karimi & Martin (1986) demonstrated that repeated bubble collapse can erode metal surfaces at rates of up to several micrometres per hour under controlled laboratory conditions, forming pits that coalesce into large-scale material loss. Lauterborn & Kurz (2010) quantified that single bubble collapse can produce audible acoustic transients capable of exciting structural resonances. Laguna-Camacho *et al.* (2013) further showed that even small differences in material hardness or microstructure can result in dramatically different erosion rates, highlighting the vulnerability of engineering alloys to cavitation. In addition to material erosion, bubble collapse generates strong pressure pulses and high-frequency noise. Li *et al.* (2018) experimentally confirmed that such pressure fluctuations can induce vibrations large enough to compromise pump and turbine performance, accelerate fatigue and increase maintenance costs. Despite these harmful effects, cavitation bubble collapse can also offer benefits when properly controlled. Gensheng *et al.* (2005) demonstrated experimentally that controlled bubble collapse near rock surfaces enhances drilling efficiency by generating localised high-pressure pulses that fragment rock without mechanical contact. Maeda *et al.* (2016) developed numerical models to optimise bubble-induced pressure pulses in petroleum wells, showing that tuning bubble size and collapse timing can significantly improve penetration rates while minimising unintended erosion. In ultrasonic cleaning applications, Reuter *et al.* (2017) quantified how an acoustic cavitation bubble removes membrane fouling and surface contaminants, demonstrating that collapse-induced microjets and pressure waves can effectively dislodge adhered particles without damaging underlying surfaces. In the background of surface engineering, Soyama, Chighizola & Hill (2021) used hydrodynamic cavitation for shotless peening, where repeated controlled bubble collapses produce uniform plastic deformation, improving metal fatigue resistance without mechanical impact or abrasive media. In biomedical contexts, particularly in dentistry, cavitation induced in the cooling water passing over the probe tip has been shown to significantly aid in plaque removal (Walmsley, Laird & Williams 1988).

Whether a cavitation effect is desirable or not, a fundamental understanding of the physics leading to these phenomenons is essential. To this end, focusing on the simplest form of cavitation, the single bubble, enables a controlled investigation of bubble dynamics without the complexity of bubble clouds. Experimental methods have been developed to generate a single vapour bubble on demand. These single bubbles can be generated by several means, most of them not implying a local pressure drop in the liquid, i.e. hydrodynamic cavitation, but by either acoustic waves termed acoustic cavitation or by local energy deposition methods.

https://doi.org/10.1017/jfm.2026.11781 Published online by Cambridge University Press

Acoustic cavitation occurs when ultrasound waves propagate through the liquid, producing a mechanical vibration that makes the dissolved gas nuclei grow to a bubble (Ashokkumar 2011). The acoustic method excites the bubble over several oscillation cycles and is widely used in the studies of cavitation enhanced chemistry and luminescence. The near-adiabatic collapse of an acoustic cavitation bubble produces extreme local temperatures and pressures, leading to the formation of highly reactive radicals, which initiate a variety of sonochemical processes, including nanomaterial synthesis, polymerisation and degradation of organic pollutants (Mišík & Riesz 1996; Rae *et al.* 2005; Ashokkumar *et al.* 2007). Moreover, acoustic cavitation has shown potential in biomedical applications, including diagnostic and therapeutic ultrasound (Tsochatzidis *et al.* 2001; Iida *et al.* 2010). However, the acoustic-induced cavitation bubble grows from pre-existing nuclei and its collapse is influenced by continuous pressure waves in the surrounding liquid, making precise control of bubble position, size and collapse time challenging. Energy deposition methods complement this by generating a single bubble precisely at the energy focus, whose collapse is driven solely by the liquid pressure. Thanks to these advantages, it is more controlled to investigate the effect of a pressure gradient on the collapse of a single cavitation bubble (Tinguely 2013).

The two main energy deposition methods used to generate the cavitation bubble in a liquid are the spark-induced and laser-induced methods. In the spark-induced method, two electrodes are immersed in the water and an electric discharge between creates a small plasma channel that rapidly expands into a vapour bubble. This approach has been extensively applied to study bubble dynamics and related physical phenomena. For instance, Avila, Song & Ohl (2015) showed that a microjet generated from a spark-induced bubble can penetrate soft material, opening possibilities for painless, needle-free drug delivery. Zhang *et al.* (2015) studied large spark-induced bubbles under buoyant conditions, providing insights into underwater explosion dynamics and cavitation-induced structural loading. Cui *et al.* (2018) employed electric discharge to generate a single bubble near ice plates, demonstrating that the resulting collapse can fracture ice and, thus, be exploited for ice-breaking applications. However, since the electrodes are placed directly within the liquid, the bubble typically forms at the electrode tip, leading to unavoidable interactions between the bubble and the electrodes. This configuration can limit control over bubble positioning and reproducibility. In contrast, the laser-induced method is non-intrusive. The laser beam can be focused through an optical system located outside the test chamber. Laser-induced cavitation is thus seen as a more practical and controllable way to create bubbles near a solid wall with minimal disturbance to the surrounding environment (Brujan *et al.* 2001; Tomita *et al.* 2002; Zwaan *et al.* 2007), which is what we intend to investigate in this study.

Motivated by this better controllability, a substantial body of experimental investigations have recently employed high-power lasers to induce cavitation bubbles near a solid wall and study the underlying mechanism in detail. Example studies in this regard include identification of the primary sources of pressure at a wall when a single bubble collapses (Zhao & Coutier-Delgosha 2023; Subramanian *et al.* 2026), morphological evolution of the cavitation bubble collapse (Zhang *et al.* 2022), change of residual wall stress with the relative distance between bubble and wall (Ren *et al.* 2016), influence of a particle on the collapsing dynamics near a solid wall, (Zhang *et al.* 2019), role of the gaseous composition within bubbles on the collapse dynamics (Preso *et al.* 2024), measurement of temperature (Dular & Coutier-Delgosha 2013), pressure (Herbert, Balibar & Caupin 2006; Subramanian *et al.* 2026) and velocity (Khlifa *et al.* 2013) in the liquid, as well as the thermodynamic effects on single cavitation bubble dynamics under various ambient temperature conditions (Phan *et al.* 2022*a*). Moreover, the influence of the relative wall distance on the damage caused by laser-induced bubble collapse, as well as the effect of

https://doi.org/10.1017/jfm.2026.11781 Published online by Cambridge University Press

boundary roughness on bubble dynamics, has been experimentally investigated. For example, Dular, Požar & Zevnik (2019) quantified the damaged volume of boundary surface produced by the collapse of a laser-induced bubble at stationary conditions for different relative wall distances, and showed that the impact of the microjet is dominant at small values of a relative wall distance, while its influence diminishes as the bubble collapses farther from the boundary. Kadivar *et al.* (2021) compared the dynamics of a single laser-induced cavitation bubble near a smooth surface and a microstructured riblet surface, demonstrating that the microstructured boundary can efficiently reduce the destructive effects of bubble collapse. Nguyen *et al.* (2025) investigated the effects of the free surface on the dynamics of a single laser-induced bubble near a rigid boundary, revealing that the presence of a nearby free surface leads to a larger bubble and more violent collapse compared with the case where the bubble is farther from the rigid boundary.

While the evolution of bubble shape can be measured by high-speed optical imaging, and the flow fields in the liquid as well as boundary effects on bubble dynamics can be quantified, experimental techniques have inherent limitations in capturing the transient internal behaviour within the bubble (e.g. distribution of fields). To overcome these constraints, numerical simulations are highly necessary to study laser-induced cavitation, focusing on the physics behind a single bubble near a solid wall.

A key novelty in this work is the use of a new computational model that combines compressible multiphase fluid dynamics with laser radiation and phase transition, capable of capturing the complete lifecycle of a single bubble near a solid boundary, i.e. from the bubble formation to its collapse. In the past, the common approach in bubble dynamics simulations was to simplify the problem by initiating the bubble from rest near a solid wall, that is, with predefined initial conditions for pressure, temperature and velocity at a given bubble size and with uniformly distributed flow fields. This simplification is typically implemented in one of two ways. The first is to start from the maximum radius to focus on the collapse phase. For instance, Fuster & Popinet (2018) proposed an all-Mach semi-implicit scheme in which a single bubble is initialised from rest with a prescribed non-dimensional maximum radius, in order to study collapse dynamics near a solid wall and capture the high-speed jet formation impacting on the wall. This method was later extended by Saade, Lohse & Fuster (2023) to account for heat transfer between phases and by Yang, Wang & Romanò (2025) to explore a wide parametric space. The second approach is to start from a small nucleus and simulate most of the expansion phase. Following this strategy, Lechner *et al.* (2020) numerically studied the distance dependence of bubble dynamics and its impact on jet formation. Gonzalez-Avila, Denner & Ohl (2021) conducted the simulation of bubble expansion as a supplement of the experimental measurements and investigated the origin of the wall pressure peak. Bußmann *et al.* (2023) numerically studied the expansion and collapse dynamics of a single cavitation bubble near a solid wall using a high-resolution sharp-interface level set method, identifying three jetting regimes. Both of these common numerical approaches rely on a major simplification, i.e. the bubble is initialised from rest with a predefined radius and simplified pressure and temperature initial conditions. In reality, cavitation bubbles nucleate through complex processes involving phase transition, intense non-equilibrium thermodynamics, rapid initial growth and a non-zero initial velocity field (Brennen 2014). These key processes are absent in simulations that start from rest with a predefined bubble. That neglects critical initial conditions that govern the early time energy partition between the liquid and vapour phases, determine the initial pressure, temperature and velocity fields, and thus, decide the bubble's subsequent dynamics. The impact of this simplification on predictive accuracy has been demonstrated in our previous work (Wang, Yang & Romanò 2026), where we considered three stand-off ratios. We found that, for the stand-off ratio

https://doi.org/10.1017/jfm.2026.11781 Published online by Cambridge University Press

of 1.82, by explicitly modelling the water breakdown phase yields the best agreement with experimental measurements of maximum wall pressure, with a relative error of only 6 %, compared with 48 % when starting from a small nucleus or 66 % from the maximum bubble size. In this work, we thus include the bubble nucleation by coupling the multiphase compressible Euler equations with a laser radiation equation that models the absorption of laser energy by the fluid flow. The algorithms and properties of this method were recently reported by Zhao, Ma & Wang (2023), together with some verification tests presented by Zhao *et al.* (2024). Additional validations of the computational method are summarised by Zhao *et al.* (2026), where the collapse of a single spherical bubble in an infinite liquid medium is simulated and compared in detail with experimental data reported by Kröninger *et al.* (2010), showing that spherical symmetry is well preserved during collapse. Related to this effort, laser-induced bubble nucleation has also been addressed at the molecular scale using molecular dynamics simulations coupled with analytical laser–liquid interaction models (Rezaee *et al.* 2025). However, such approaches are inherently restricted to nanometre spatial scales and ultrashort time scales, whereas the present framework targets millimetre scale bubble dynamics and wall-induced collapse phenomena. Linking it with continuum-scale bubble dynamics analysis is not straightforward.

Another novelty of the current study is that we apply such a method, previously used only for laser-fibre-attached cavitation and a long-pulsed laser (duration $\sim 100\,\mu$s), for the first time to carry out a detailed study on a wall-detached cavitation bubble induced by a short-pulsed laser (duration ~ 5 ns). To the best of our knowledge, there is currently no unified theory or computational model for cavitation induced by various types of lasers (duration from nanoseconds to milliseconds) while simultaneously addressing the non-uniform temperature distribution inside the bubble. The current study serves as a step towards bridging this gap. The present work explicitly resolves the cavitation inception phase, which determines the initial thermodynamic and velocity fields and strongly influences subsequent collapse dynamics. In contrast to the previous numerical studies where the bubble is initialised with prescribed or assumed initial conditions, the present approach avoids such initialisation artefacts by modelling a nucleation-consistent process. Based on this computational model, we systematically analyse the effects of the stand-off distance on laser-induced bubble dynamics and peak wall pressure, and we provide a more comprehensive and physically grounded understanding of the collapse process by comparing with experimental measurements by Subramanian *et al.* (2026).

The paper is organised as follows: § 2 details the governing equations and problem formulation for laser-induced cavitation bubble; § 3 outlines the numerical methodology and presents the convergence study; § 4 validates the model through the comparison with experimental measurements on interfacial dynamics and peak wall pressure; § 5 compares the three collapse regimes identified in both simulations and experiments; § 6 analyses the bubble dynamics for three selected stand-off ratios; § 7 examines the internal bubble dynamics, including temperature, pressure, velocity and density. Finally, we present the conclusion and future outlook.

2. Problem formulation

2.1. *Problem description*

In the experiment performed by Subramanian *et al.* (2026), a Q-switched Nd: YAG laser (Big Sky Laser PN00148300) with a wavelength of 532 nm, maximum pulse energy of 200 mJ and a pulse duration of 5 ns was used as the energy source to induce the cavitation bubble. The experiment was carried out in a $20.3 \times 20.3 \times 20.3\,\text{cm}^3$ glass tank filled with pure water under ambient conditions. Figure 1 presents a series of high-speed images that

https://doi.org/10.1017/jfm.2026.11781 Published online by Cambridge University Press

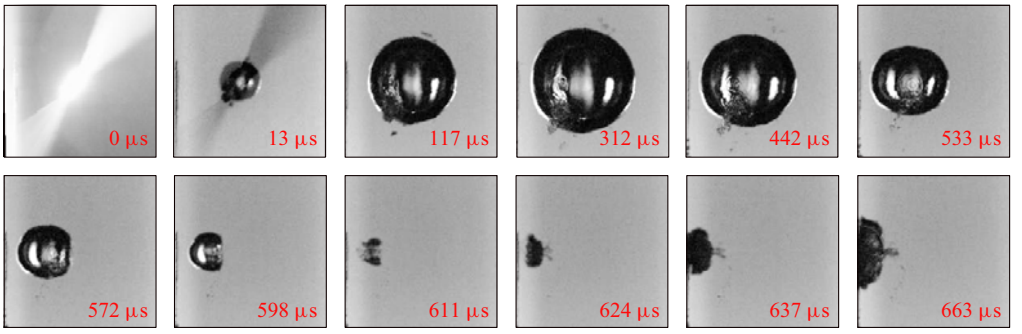


Figure 1. Experimental visualisations of bubble evolution near the wall obtained by Subramanian *et al.* (2026). The wall is aligned with the left boundary in each subfigure.

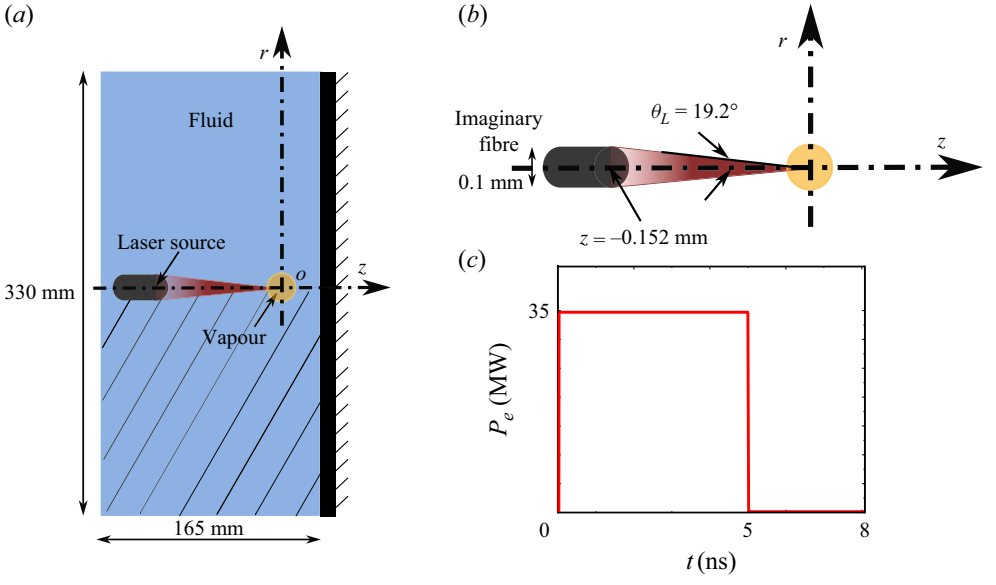


Figure 2. Schematic of laser-induced bubble generation. (*a*) Computational domain with axisymmetry. (*b*) Geometry of the laser radiation domain. (*c*) Temporal profile of laser power.

show the nucleation and evolution of a cavitation bubble near a wall. The bubble becomes visible at about 13 μs from laser focusing. It expands continuously until its maximum size is reached at around 312 μs before shrinking to collapse at approximately 611 μs from nucleation. We stress that this study does not include a comparison between experimental and numerical results during the rebound phase, as phase change is known to be significant starting from the first rebound phase (Yin *et al.* 2021; Phan *et al.* 2022*a*), and the present model does not include phase transition beyond bubble generation.

Figure 2 shows the set-up of the simulation. To replicate the experimental conditions in our computational model, we employed an axisymmetric simulation domain with a radius and length of 165 mm shown in figure 2(*a*), 55 times the maximum bubble radius of around 3 mm to avoid the impact of the computational boundary on bubble shape and size by constraining its growth. In our simulations, r denotes the radial coordinate and z the axial coordinate. Regarding the boundary conditions, the wall near the cavitation bubble is considered rigid. Non-slip and no-penetration conditions are therefore applied,

https://doi.org/10.1017/jfm.2026.11781 Published online by Cambridge University Press

and we assume that the wall is also adiabatic. The far-field boundary conditions at $r = r_\infty$ and $z = -z_\infty$ are set as Neumann conditions, ensuring that outgoing waves do not reflect back. The symmetry boundary condition is enforced along the axis $r = 0$ at which the laser beam is focused. The laser, positioned outside the water tank in the experiment, is modelled as originating at $z = -0.152$ mm, with a laser source radius of $R_L = 0.05$ mm and a convergence angle of $\theta_L = 19.2°$, consistent with the laboratory experiment, as shown in figure 2(*b*).

The initial conditions assume that the domain is filled solely with liquid water of density $\rho_0 = 1000\ \mathrm{kg\ m^{-3}}$, pressure $p_0 = 1$ atm and temperature $T_0 = 293.15$ K. The water is initially assumed at rest. In the computational model, the spatial distribution of laser intensity is simplified and treated almost as a square wave, as shown in figure 2(*c*). The laser power P_e increases rapidly to its peak of around 35 MW within 0.01 ns, remains constant for 5 ns and then decreases to zero over 0.02 ns. Given the high intensity of the short-pulse laser, energy loss while beam travelling through water is accounted for by adopting a nonlinear absorption coefficient, which is a function not only of the wavelength of the laser but also its intensity. The energy loss in water is approximately 6 % for beam travel distances less than 100 mm (Rockwell *et al.* 1993; Marble *et al.* 2018). The absorption coefficient, $\alpha(I)$, is expressed as

$$\alpha(I) \approx \alpha(0) + \beta I, \tag{2.1}$$

where $\alpha(0)$ is the linear absorption coefficient, set to $4.47 \times 10^{-2}\ \mathrm{m^{-1}}$ (Pope & Fry 1997), and β is the nonlinear absorption coefficient in $\mathrm{m\ W^{-1}}$, estimating $\beta < 4 \times 10^{-14}\ \mathrm{m\ W^{-1}}$. The laser intensity is represented by I in $\mathrm{W\ m^{-2}}$. In our simulation, the absorption coefficient α is set to $10^5\ \mathrm{m^{-1}}$ for liquid water and $10^{-5}\ \mathrm{m^{-1}}$ for the vapour, which forms the basis of the current numerical study, though it is acknowledged that the absorption measurements involve uncertainty, necessitating reasonable approximations. The vaporisation temperature and latent heat of vaporisation are specified as $T_{vap} = 373.15$ K and $l = 2256.4\ \mathrm{J\ g^{-1}}$, respectively.

2.2. *Governing equations*

As reported in Yang *et al.* (2025), the influence of viscosity and surface tension on the bubble dynamics near a wall is negligible for millimetric bubble collapse like ours. The equations governing compressible two-phase flows that neglect the effects of viscosity and surface tension while accounting for radiative heat transfer are used in this study, i.e.

$$\frac{\partial \boldsymbol{W}(\boldsymbol{x}, t)}{\partial t} + \boldsymbol{\nabla} \cdot \mathcal{F}(\boldsymbol{W}) = \boldsymbol{\nabla} \cdot \mathcal{G}(\boldsymbol{W}), \tag{2.2a}$$

with

$$\boldsymbol{W} = \begin{bmatrix} \rho \\ \rho \boldsymbol{V} \\ \rho e_t \end{bmatrix}, \qquad \mathcal{F} = \begin{bmatrix} \rho \boldsymbol{V}^T \\ \rho \boldsymbol{V} \otimes \boldsymbol{V} + p \boldsymbol{I} \\ (\rho e_t + p)\, \boldsymbol{V}^T \end{bmatrix}, \qquad \mathcal{G} = \begin{bmatrix} \boldsymbol{0}^T \\ \boldsymbol{0} \\ \left(k \boldsymbol{\nabla} T - \boldsymbol{q_r}\right)^T \end{bmatrix}, \tag{2.2b}$$

where ρ, $\boldsymbol{V}$, p and T denote the fluid's density, velocity, pressure and temperature fields, respectively. The total energy per unit mass, e_t, is defined as

$$e_t = e + \frac{1}{2} |\boldsymbol{V}|^2, \tag{2.3}$$

where e represents the fluid's internal energy per unit mass. The thermal conductivity coefficient k is set to $0.5576\ \mathrm{W\ mK^{-1}}$ for liquid and $0.02457\ \mathrm{W\ mK^{-1}}$ for vapour, and $\boldsymbol{q_r}$ refers to the radiative heat flux induced by the laser.

https://doi.org/10.1017/jfm.2026.11781 Published online by Cambridge University Press

Reference	Phase	γ	C_p (J/(kg K))	p_c (Pa)	b (m^3 kg^{-1})	q (J kg^{-1})
Zein *et al.* (2013)	$i=0$	2.057	7094.59	1.066×10^9	0	-1994.674×10^3
	$i=1$	1.327	1592.4	0	0	1995×10^3
Métayer *et al.* (2016)	$i=0$	1.19	5099.15	7.028×10^8	6.61×10^{-4}	-1177.788×10^3
	$i=1$	1.47	1403.85	0	0	2077.616×10^3

Table 1. NASG EoS parameters and thermodynamic properties for the liquid water and water vapour phase.

To close the governing equations (2.2*a*), an equation of state (EoS) for each phase, including a temperature equation, is required. In this study, the Noble–Abel stiffened gas (NASG) equations are employed for both phases introducing the following pressure and temperature equations (Métayer *et al.* 2016):

$$p = (\gamma_i - 1)\frac{e - q_i}{\rho^{-1} - b_i} - \gamma_i p_{ci}, \tag{2.4a}$$

$$T = \frac{\gamma_i}{C_{pi}}\left(e - q_i - \left(\frac{1}{\rho} - b_i\right)p_{ci}\right). \tag{2.4b}$$

Here the subscript i refers either to the liquid water ($i=0$) or to the water vapour ($i=1$). For each phase, γ, p_c, q and b are constant parameters that characterise its thermodynamic properties. Specific heat capacity at constant pressure, denoted by C_p, is assumed to be a constant. Employing the NASG EoS, the corresponding speed of sound c is expressed as

$$c = \sqrt{\frac{\gamma_i(p + p_{ci})}{\rho(1 - \rho b_i)}}. \tag{2.5}$$

Hyperbolicity requires only that $p > -p_{ci}$, which allows for negative pressure in the liquid phase. Two groups of EoS parameter values are tested in this study, as shown in table 1. A sensitivity analysis to these parameters is reported in Appendix A, indicating that the adoption of the parameters from Zein, Hantke & Warnecke (2013) provides a better match with the experimental measurements by Subramanian *et al.* (2026), which is therefore used in the following simulations.

The laser radiation equation is derived based on energy conservation, taking into account the assumptions that the laser radiation dominates over the black-body radiation and that the laser propagates in a fixed direction with a certain wavelength (Zhao *et al.* 2023):

$$\nabla\cdot(L\boldsymbol{s}) = \nabla L\cdot\boldsymbol{s} + (\nabla\cdot\boldsymbol{s})L = -\alpha(I)L, \tag{2.6a}$$

$$\boldsymbol{q}_r = L\boldsymbol{s}. \tag{2.6b}$$

Here s denotes the direction of the laser propagation and L represents the laser radiance, which can be calculated for a uniform beam as

$$L = \frac{P_e(1 + \cos\theta_L)}{\pi R_L^2}. \tag{2.7}$$

Our initial condition considers pure liquid water to generate the laser-induced water vapour. The phase transition process is accomplished when the intermolecular potential energy in the liquid phase reaches the latent heat, as shown in figure 3. The fundamental idea of the method used in this study is to introduce a new variable, namely the latent heat reservoir Λ, to track and store the intermolecular potential energy in the liquid phase.

https://doi.org/10.1017/jfm.2026.11781 Published online by Cambridge University Press

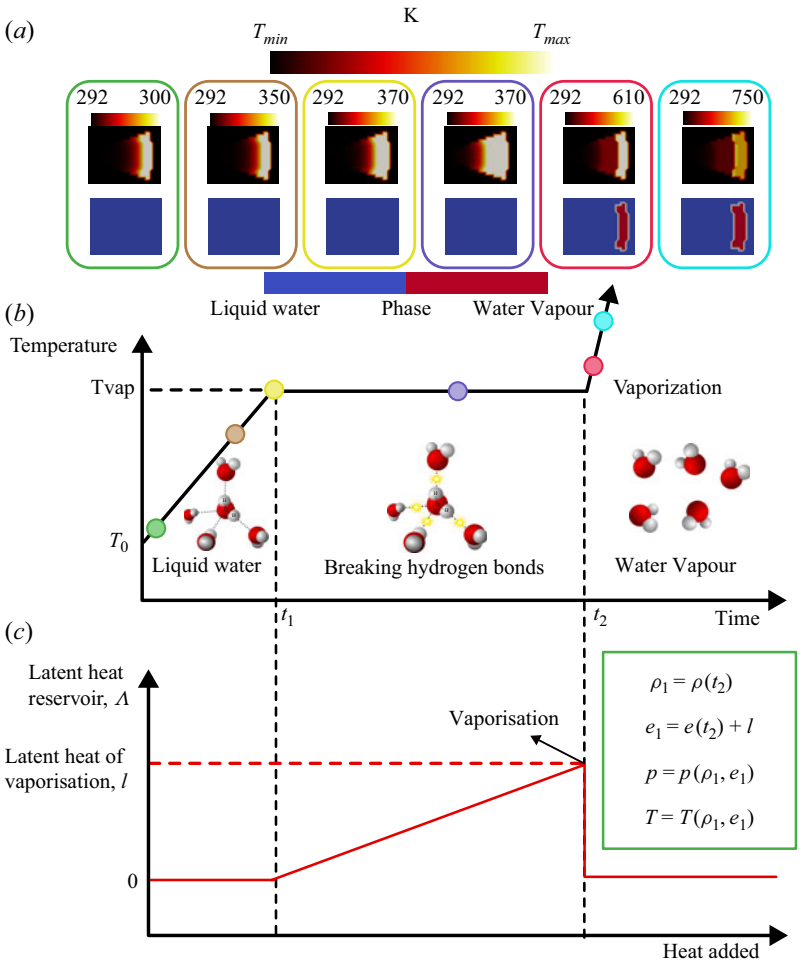


Figure 3. Predicting laser-induced vaporisation by the method of latent heat reservoir. (*a*) Temperature field and phase distribution. The phase field shows that the computational domain is initially filled with liquid water. The coloured frames correspond to the time instants indicated by circles of the same colour in (*b*). (*b*) Temporal evolution of the liquid water temperature. Coloured circles correspond to subfigures in (*a*). (*c*) Accumulation of additional energy in the latent heat reservoir.

The vaporisation temperature T_{vap}, and latent heat l, are assumed to be constant and used as a coefficient in the method. Figure 3(*a*) shows the temperature and phase fields in the vicinity of the laser focal region during the ultra-early stage of bubble generation. The computational domain is initially filled with liquid water at the initial temperature T_0. Owing to the highly localised laser energy deposition, a rapid rise in maximum temperature first occurs near the laser plane (on the right-hand side of each snapshot) and subsequently propagates towards the laser focus. Phase transition is induced within approximately 0.01 ns near the laser plane, with the vapour phase propagating along the same path as the temperature, marking the onset of bubble nucleation and early growth. The videos of the temperature, pressure, density, velocity and laser radiation field during this early stage can be found as supplementary movies available at https://doi.org/10.1017/jfm.2026.11781. When the vaporisation temperature T_{vap} is reached, the maximum temperature in the liquid no longer rises, even though the laser

https://doi.org/10.1017/jfm.2026.11781 Published online by Cambridge University Press

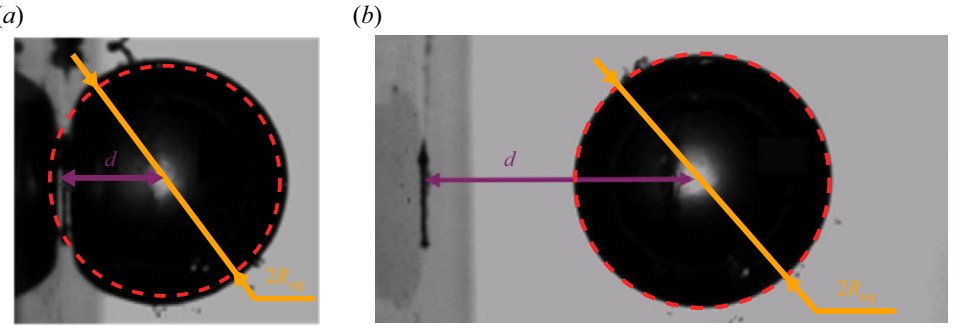


Figure 4. Bubble at stand-off ratio γ (*a*) smaller and (*b*) larger than 1. The red dashed lines represent the spherical bubble with a volume equal to the cavitation bubble's maximum volume.

continues to supply energy as shown in figure 3(*b*). At this stage, a new variable Λ is activated to store the additional absorbed energy as shown in figure 3(*c*). This stored energy models the energy needed to break the hydrogen bonds of water. When Λ reaches latent heat l, the phase transition occurs at t_2. After vaporisation, the stored energy is released and contributes to the initial internal energy of water vapour $e(t_2)$. The total initial internal energy of the water vapour is therefore $e_1 = e(t_2) + l$ and the density is $\rho_1 = \rho(t_2)$. The pressure and temperature immediately after phase transition are then obtained naturally from the EOS of the water vapour $p = p(\rho_1, e_1)$ and $T = T(\rho_1, e_1)$. It is worth noting that non-equilibrium interfacial phase-change processes, such as condensation, may influence cavitation dynamics. However, such effects are not included in the present model, as this study is at the millimetric scale, for which previous studies have shown that inertial dynamics dominate the overall bubble motion. In particular, phase transition affects millimetric bubble dynamics only after the first collapse stage (Yin *et al.* 2021; Phan *et al.* 2022*b*). Incorporating detailed non-equilibrium phase-change models is therefore beyond the scope of the present work and is left for future investigations. We further stress the work by Zhao *et al.* (2023) as a motivation for our modelling assumptions.

The bubble dynamics can be analysed using two key parameters: the equivalent radius, denoted as R_{eq}, and the distance from the bubble's centroid to the solid wall, d (see figure 4). The stand-off ratio, expressed as

$$\gamma = \frac{\mathrm{d}(t_{MR})}{\max\limits_{t}(R_{eq})}, \tag{2.8}$$

quantifies the relative distance between the bubble's centroid and the wall, where t_{MR} refers to the time when the bubble reaches its maximum equivalent radius. In this study, we investigate the influence of the stand-off ratio $\gamma \in [0.79, 2.14]$ on the bubble dynamics, including the interfacial dynamics, pressure, temperature and velocity fields.

3. Numerical method

3.1. *Numerical schemes*

In this section we present a summary of the numerical schemes used; see Zhao *et al.* (2023) for a detailed description. The compressible two-phase Euler equations are solved using a node-centred finite volume formulation combined with the finite volume method with exact two-phase Riemann solvers. The interfacial fluxes across liquid–vapour boundaries are computed by constructing and solving one-dimensional bimaterial

https://doi.org/10.1017/jfm.2026.11781 Published online by Cambridge University Press

Riemann problems, while within each phase, the well-known monotonic upstream-centred scheme for conservation laws is employed for spatial reconstruction and a second-order explicit Runge–Kutta method for time integration.

The liquid–vapour interface is captured using a localised level set method, which solves the level set equation

$$\frac{\partial \phi}{\partial t} + \boldsymbol{V} \cdot \nabla \phi = 0, \tag{3.1}$$

only in a narrow band surrounding the interface to reduce the cost. The level set function ϕ is reinitialised periodically by solving

$$\frac{\partial \phi}{\partial \tilde{t}} + S(\phi_0)\,(|\nabla \phi| - 1) = 0 \tag{3.2}$$

to restore the signed-distance property $|\nabla \phi| = 1$. Here, $\tilde{t}$ is a fictitious time variable. The level set function before reinitialisation is denoted by ϕ_0, and $S(\phi_0)$ is a smoothed sign function, given by

$$S(\phi_0) = \frac{\phi_0}{\sqrt{\phi_0^2 + \varepsilon^2}}, \tag{3.3}$$

where ε is a constant coefficient, set to the minimum element size of the mesh. Phase transition is handled consistently by resetting the sign of ϕ in control volumes that satisfy the vaporisation criterion, determined from a latent heat reservoir model that accumulates absorbed energy until the latent heat l is reached (see figure 3). The reinitialisation of the level set function is, in general, not strictly mass conservative and may introduce small shifts of the zero level set at the discrete level. In the present work, reinitialisation is performed only within a narrow band around the interface and is initialised from the pre-reinitialised field, for which the zero level set is theoretically preserved. Moreover, upon vaporisation, the local phase indicator is switched, and the internal energy is updated through an isochoric process that conserves both mass and energy. The laser radiation transport is described by a reduced, monochromatic, directional form of the radiative transfer equation and discretised using a finite volume method on the same mesh as the fluid solver. The above numerical methods are implemented using the M2C solver (https://github.com/kevinwgy/m2c, Zhao *et al.* 2026), which is employed to carry out the simulations reported in this paper.

3.2. *Spatial convergence study*

The influence of mesh refinement is investigated to identify an optimal mesh size that ensures convergence in the bubble generation. The spatial convergence study is divided into global and local parts. Firstly, for the global convergence study, the axisymmetric computational domain is 330 mm × 165 mm as mentioned above. Since the bubble induced by the laser has an experimental radius of approximately 3 mm, a subregion of 9 mm × 8 mm is designated with finer mesh resolution than the surrounding area. Only the mesh size within this designated region is varied, while the mesh outside remains unchanged (see figure 5). Seven cases for $\gamma = 1.82$ are examined, with a minimum cell size from $\Delta x = 4.5 \times 10^{-6}$ m to $\Delta x = 10^{-5}$ m. As the computational domain is initially filled with liquid water, a bubble is generated and simulated numerically on our discrete grid. Suppose that the mesh near the nucleation site is not well refined, the initial bubble configuration will vary between simulations, leading to different initial conditions and, thus, non-comparable results. This makes it essential to fix the mesh near the nucleation

https://doi.org/10.1017/jfm.2026.11781 Published online by Cambridge University Press

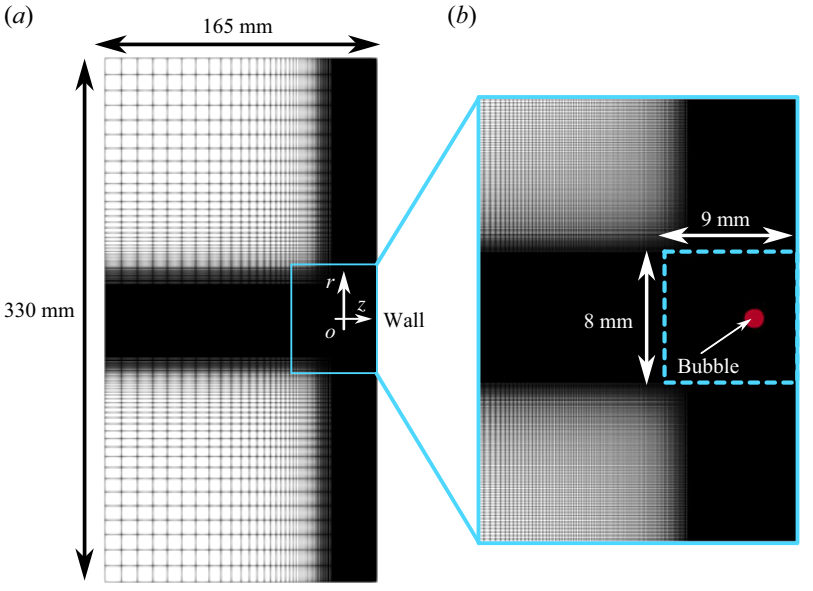


Figure 5. Global mesh distribution.

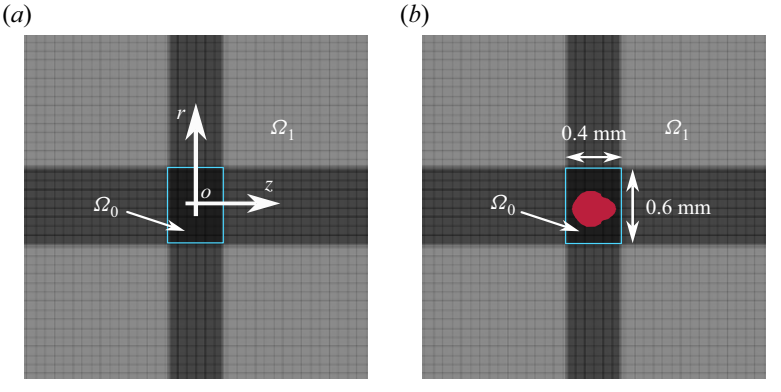


Figure 6. Local mesh distribution near the bubble nucleation site: (*a*) $t = 0$ s, (*b*) $t = 10^{-7}$ s. The red area within Ω_0 represents the bubble right after its nucleation.

site across our comparative study in order to ensure repeatability and consistency across different simulations. For the local convergence study, the focus is on the region of bubble nucleation of 0.4 mm × 0.6 mm, denoted by Ω_0 where the mesh size of $\Delta x = 5 \times 10^{-6}$ m was determined to be optimal from the part of the global convergence study. Outside this space Ω_1, the mesh size varies among $\Delta x = 2 \times 10^{-5}$ m, 10^{-5} m and 5×10^{-6} m, but the bubble will always form within the the extra fine mesh near the nucleation site (see figure 6). The details of both the global and local convergence studies are reported in our previous paper (Wang *et al.* 2026), where the sensitivity of the equivalent bubble radius and maximum wall pressure to the spatial mesh refinement have been demonstrated.

Here, we extend this analysis by including the pressure and temperature fields, together with the bubble shape as the supplementary validation for the local influence of mesh resolution. The results are compared at three different mesh sizes at $t = 2 \times 10^{-7}$ s (see figure 7), corresponding to the moment when the bubble has just expanded beyond

https://doi.org/10.1017/jfm.2026.11781 Published online by Cambridge University Press

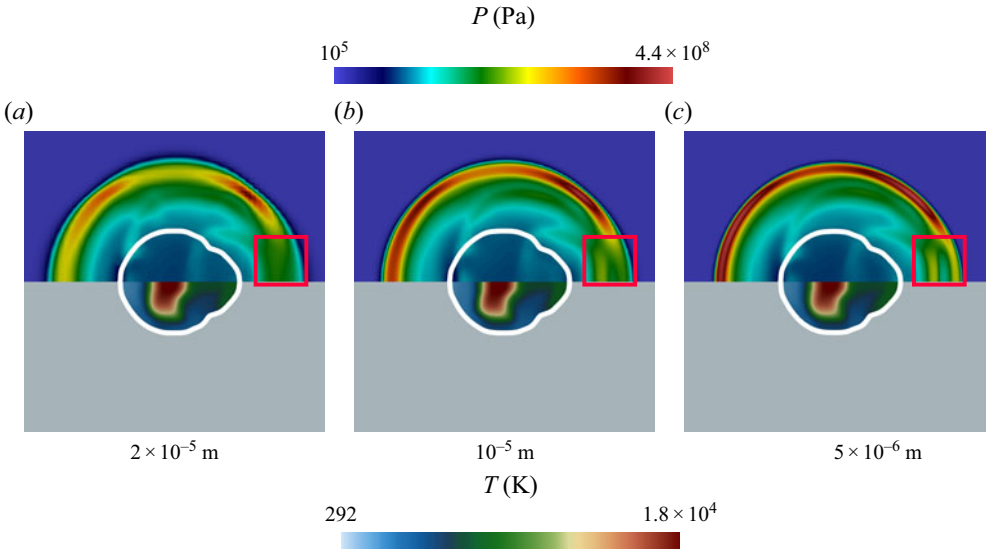


Figure 7. Pressure (on the top) and temperature (on the bottom) fields at $t = 2 \times 10^{-7}$ s for three levels of mesh refinement. The bubble shape is represented in white. For all three simulations, the grid spacing within Ω_0 is fixed at $\Delta x = 5 \times 10^{-6}$ m, while the mesh size within Ω_1 varies from $\Delta x = 2 \times 10^{-5}$ m to 5×10^{-6} m.

the finely meshed nucleation region Ω_0 and starts interacting with the coarser mesh in Ω_1, which makes it a physically relevant and sensitive time for examining the effect of mesh refinement. From figure 7 it can be seen that the mesh refinement has negligible influence on the temperature field and bubble shape. It is worth noting that upon an increase of the numerical domain, we do not observe any significant change in the bubble size during the early stage. Besides, the bubble elongates along the laser irradiation direction and is therefore non-spherical during the early stage, showing that the side closer to the laser plane is slightly wider than the opposite side at the nucleation point, which is consistent with the experimental observation by Gonzalez-Avila *et al.* (2021), further validating the robustness of the model used in the present study, details shown in Appendix C. However, differences are observed in the pressure field. The maximum pressure in the fluid for $\Delta x = 2 \times 10^{-5}$ m within Ω_1 is around 3.3×10^8 Pa, compared with around 4.3×10^8 Pa for $\Delta x = 10^{-5}$ m and 4.4×10^8 Pa for $\Delta x = 5 \times 10^{-6}$ m. Besides, the coarsest mesh fails to fully capture the pressure distribution (see red squares in figure 7). After compromising both the computational cost and the accuracy, we thus identified an optimal mesh size of $\Delta x = 5 \times 10^{-6}$ m within Ω_0 and 10^{-5} m within Ω_1 to conduct the following simulations presented in this study. Further quantitative justifications are reported in Wang *et al.* (2026).

4. Results and discussion

4.1. *Qualitative comparison with experiments for the interfacial dynamics*

Firstly, a qualitative comparison of the bubble interface morphology is presented for five selected stand-off ratios out of the nine we study, i.e. $\gamma = 0.79$, 1.13, 1.46, 1.82 and 2.14 in figure 8. Overall, the simulated bubble shape shows excellent agreement with experiment across all cases. This agreement is particularly strong during the growth phase and the initial stages of collapse. Slight discrepancies emerge near the point of collapse, i.e. $t - t_c = 0$. Particularly for the moderate stand-off ratio $\gamma = 1.46$, a difference in the bubble shape is observed in the late collapse phase (after $t - t_c = -13$ µs). The simulation

https://doi.org/10.1017/jfm.2026.11781 Published online by Cambridge University Press

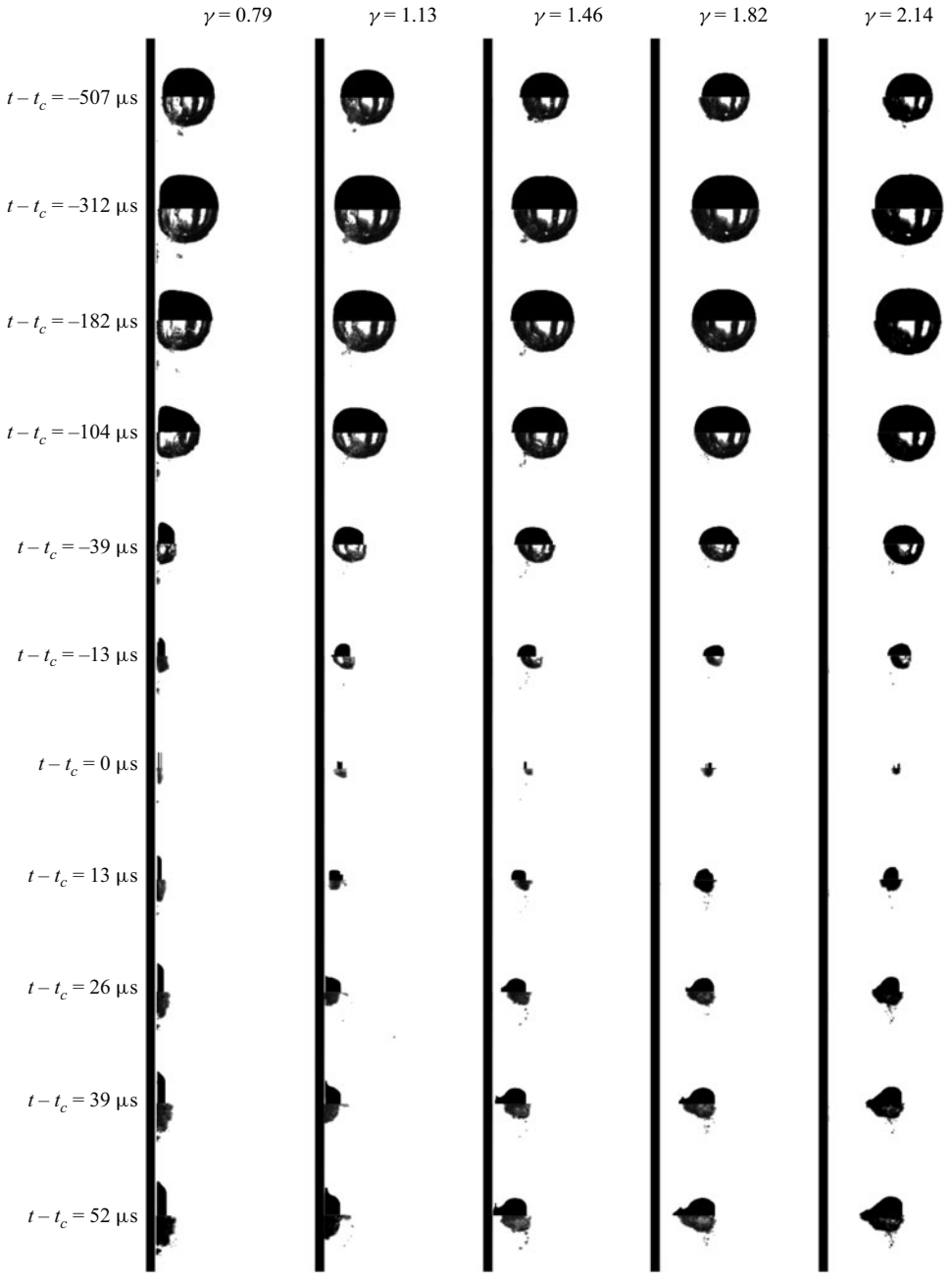


Figure 8. Bubble shape evolution at five different stand-off ratios. The collapse time of the bubble is denoted by t_c. In snapshots, the upper half is the bubble interface in 2D simulations, while the lower half is the experiment by Subramanian *et al.* (2026). The wall in black aligns with the left boundary of each snapshot.

indicates a tendency for the bubble to migrate closer to the wall compared with the experiment. This might be due to a stronger microjet, which results in a shift of the collapse time. Such an effect is quantified by the comparison of bubble lifetime in figure 9(*d*).

https://doi.org/10.1017/jfm.2026.11781 Published online by Cambridge University Press

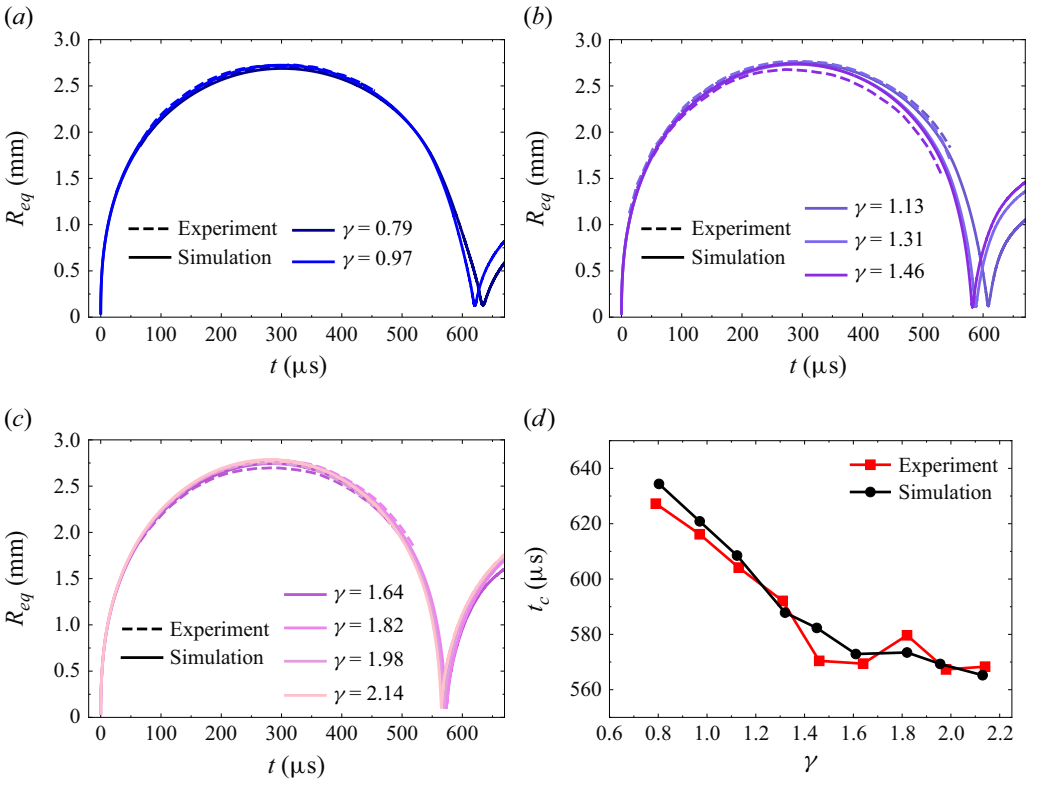


Figure 9. (*a–c*) Equivalent radius for nine stand-off ratios γ from simulations compared with the experiment by Subramanian *et al.* (2026) (dashed line). The results are further grouped into three subfigures according to the three collapse regimes identified by Subramanian *et al.* (2026), with each subfigure presenting the data for a specific regime. (*d*) The comparison in terms of collapse time t_c measured from bubble generation.

Following the qualitative comparison of the bubble interface morphology, a comprehensive quantitative analysis is performed using several key metrics: (i) the equivalent radius evolution and the corresponding collapse time, (ii) the maximum length of the bubble in the axial (z) and radial (r) directions, which are $max(\Delta z_s)$ and $max(D_s)$, (iii) the minimum and maximum position of the bubble interface on the z axis, (iv) the bubble centroid location computed assuming a uniform density inside the gas, (v) the far-wall and near-wall interface velocity.

The equivalent radius is measured from the top view using high-speed imaging following a five-step procedure (see Yang *et al.* 2025). Relevant frames are extracted from the recordings and in each frame the bubble interface coordinates (r_b, z_b) are identified based on the refractive index contrast between liquid water and vapour. Assuming axisymmetric growth, the detected interface is reflected about the symmetry axis. The details can be found in Appendix D.

The comparison of the equivalent radius (figure 9*a–c*) shows excellent agreement with the deviation in maximum bubble size being less than 2.3 % for all stand-off ratios γ. The rates of expansion and shrinkage are also well captured by the simulation, leading to collapse times t_c that align closely with experimental measurements (figure 9*d*), while a minor deviation is noted for $\gamma = 1.31$ at $t > 300\,\mu s$ where the experimental bubble collapses slightly slower than in the simulation.

https://doi.org/10.1017/jfm.2026.11781 Published online by Cambridge University Press

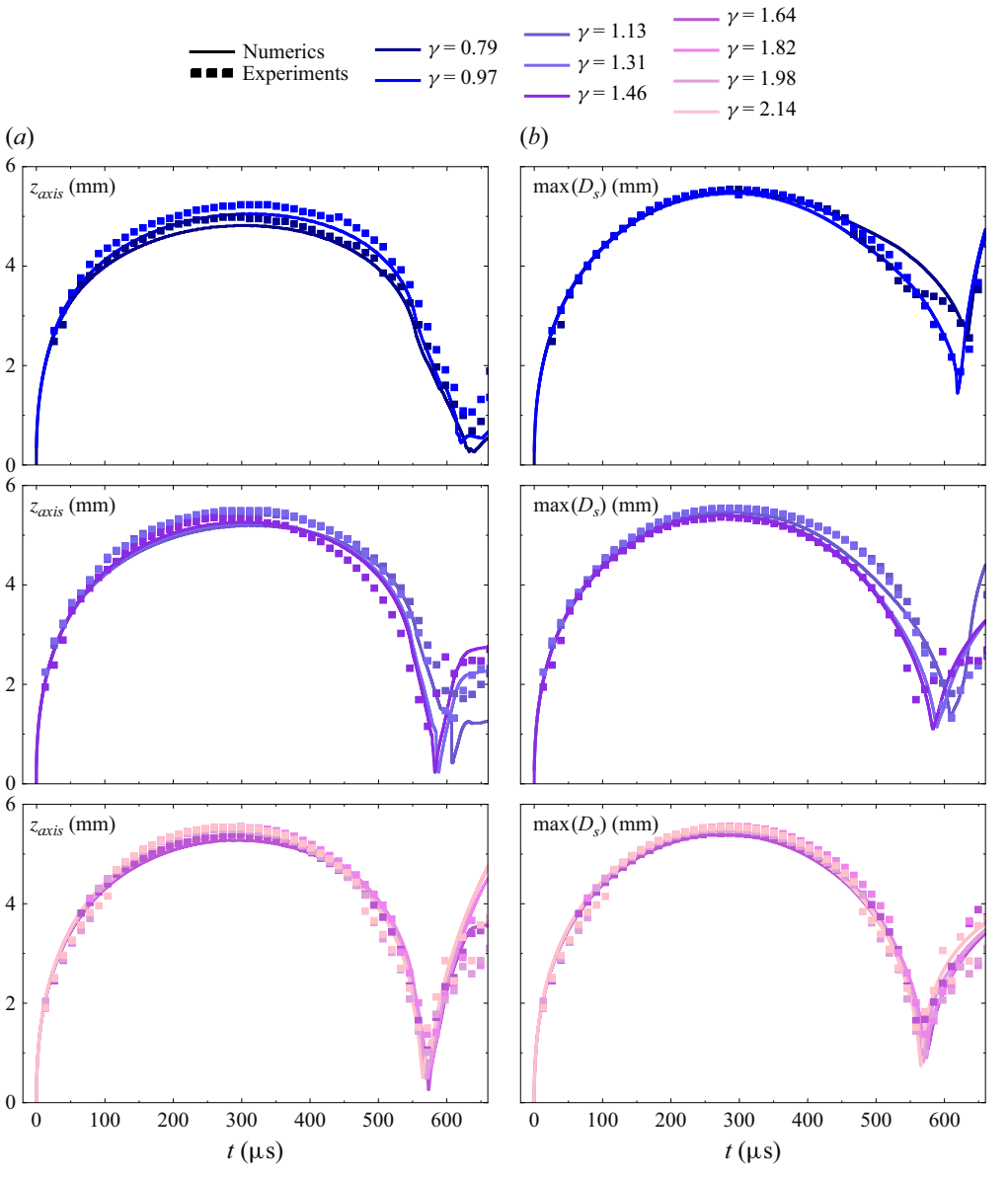


Figure 10. Comparison of the maximum bubble length in the axial direction, denoted by z_{axis} (right panel) and radial direction, denoted by $max(D_s)$ (left panel). The results are further grouped into three subfigures for each quantity according to the three collapse regimes identified by Subramanian *et al.* (2026), with each subfigure presenting the data for a specific regime.

This strong agreement extends to the geometric dimensions of the bubble. The simulated maximum lengths in the axial (z) and radial (r) directions (figure 10) closely match the experimental data across all phases of evolution, with this agreement being particularly strong for larger γ. The results reveal that the collapse phase is dominated by a rapid contraction along the z axis. This axial dominance is more pronounced for smaller stand-off ratios. Furthermore, the movement of the bubble interface on the z axis, detailed in figure 11(a), shows that the far-wall interface accelerates towards the bubble centroid more

https://doi.org/10.1017/jfm.2026.11781 Published online by Cambridge University Press

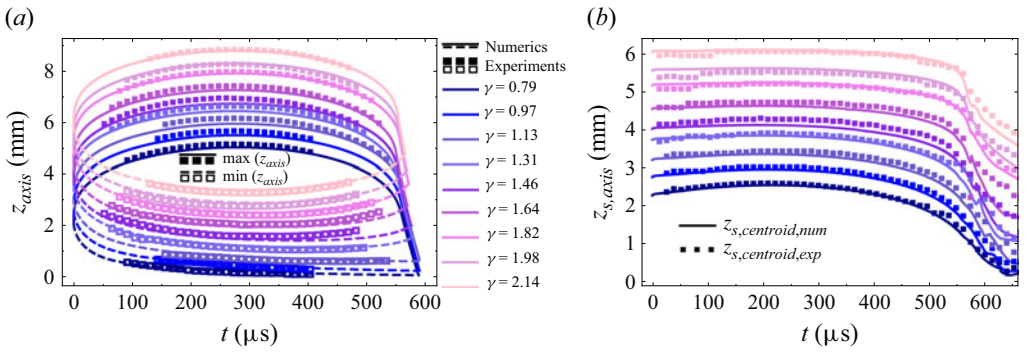


Figure 11. (*a*) Minimum and maximum location of the bubble interface on the z axis. (*b*) Comparison of the bubble centroid location.

rapidly than the near-wall interface moves towards the wall as collapse approaches. This asymmetry in interface dynamics is a key mechanism driving the development of the high-speed jet directed toward the wall.

The migration of the bubble centroid, presented in figure 11(*b*), is also accurately predicted. In both cases, the bubble migrates toward the wall for all stand-off ratios γ. For larger γ, the bubble remains relatively stable and centrally located for a longer duration before collapse owing to the weaker attractive force from the distant wall. However, once the collapse phase begins, the bubble with a larger γ migrates toward the wall more rapidly with reduced inertial resistance.

Finally, the interfacial velocities provide a critical validation metric of the inertial effects, especially prior and post collapse. The experimental study by Subramanian *et al.* (2026) provides measurements of the near-wall U_{nw} and far-wall U_{fw} interface velocities for eight stand-off ratios. A direct comparison is presented in figures 12 and 13. A discernible discrepancy in the far-wall interface velocity U_{fw} is observed in figure 12. Slight deviations occur for $\gamma = 0.79$ and 0.97, while a more significant underestimate of the experimental results is observed for $\gamma = 1.13$ and 1.31. For these cases, the underestimation of U_{fw} occurs specifically near the collapse point $t - t_c = 0$, where the bubble reaches its minimal size with a radius of approximately 0.5 mm. This scale poses exceptional challenges for the accurate experimental measurement of interface velocity. Considering the sensitivity of the interfacial velocity to the amount of energy absorbed initially, additional simulations were performed using the calibrated absorption coefficient (see cyan curves in figure 12). The absorption coefficient used for these simulations are 75 000 m^{-1} for $\gamma = 1.13$ and 73 000 m^{-1} for $\gamma = 1.31$. For $\gamma = 1.13$, the adjusted simulation yields an improved agreement with experimental data near the collapse phase. The agreement remains partially satisfactory, suggesting that the mismatch previously observed was partly due to the mismatch of absorption coefficient. In contrast, for $\gamma = 1.31$, the modification produces only minor changes, indicating that the residual differences are likely not attributable to the absorption coefficient itself. As noted by Subramanian *et al.* (2026), these deviations are likely attributable to the inevitable measurement errors associated with experimental visual capturing of high-speed, small-scale phenomena near a solid boundary. Moreover, the mixed tip-and-torus collapse regime is particularly sensitive. For instance, the experiments reported in Yang *et al.* (2025), when compared with those by Subramanian *et al.* (2026), show significant quantitative deviations for the mixed regime, even if the two studies used the same experimental set-up. This observation highlights the intrinsic difficulty of quantitatively reproducing the mixed regime not just numerically, but also experimentally.

https://doi.org/10.1017/jfm.2026.11781 Published online by Cambridge University Press

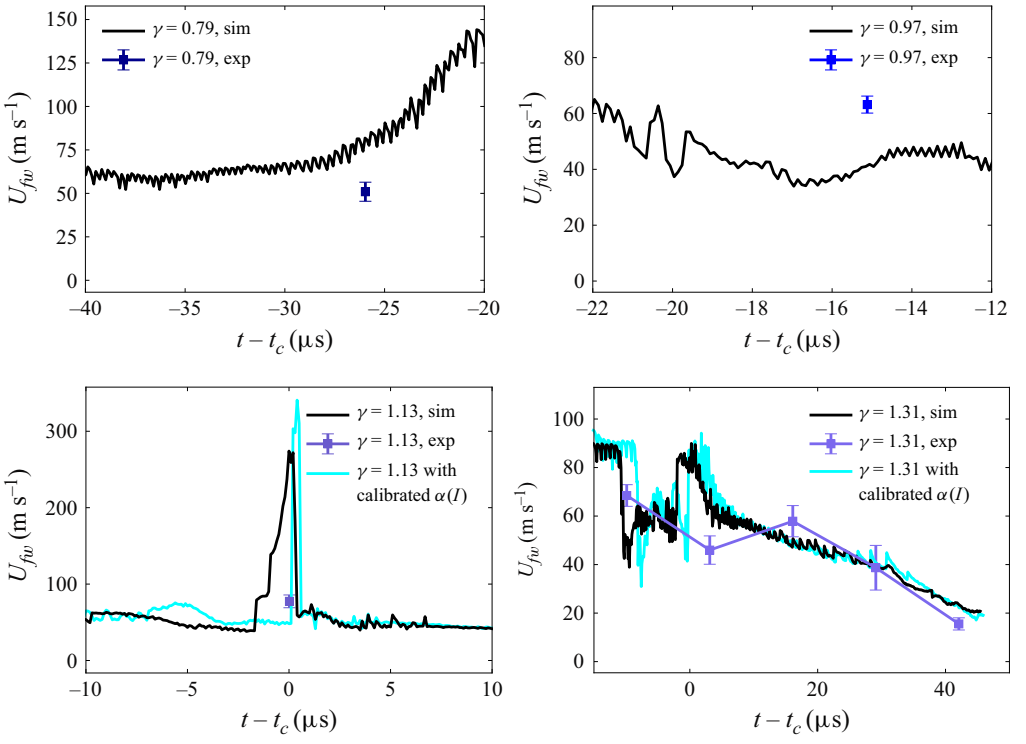


Figure 12. Comparison of the far-wall interface velocity U_{fw}. The absorption coefficient is denoted by $\alpha(I)$.

Conversely, the near-wall interface velocity U_{nw}, presented in figure 13, exhibits excellent agreement across most of the tested stand-off ratios. The simulations successfully capture both the temporal evolution and the magnitude of U_{nw}, which consistently ranges between 8–80 m s^{-1}, matching the experimental data. This robust agreement on U_{nw} is particularly significant as it confirms the model's ability to accurately capture the jetting process, which is one of the most critical aspects of the collapse dynamics.

However, a notable deviation is observed for $\gamma = 1.46$. After approximately $t - t_c = 50\,\mu$s, the simulated velocity increases while the experimental data decreases. This discrepancy arises because the bubble jet in the simulation impacts the wall earlier during the rebound phase than observed experimentally (see $\gamma = 1.46$ after $t - t_c = 52$ in figure 8). Following this earlier impact, the far-wall interface begins to accelerate toward the wall, making the onset of the second collapse phase. The propagation and accumulation of this momentum from the far-wall interface toward the rigid boundary result in a characteristic increase in the near-wall interface velocity U_{nw} seen in the simulations. Similarly to U_{fw}, an additional simulation with the adjusted absorption coefficient of 71 400 m^{-1} for $\gamma = 1.46$ is performed. Although the calibrated case does not eliminate all discrepancies, it captures a non-monotonic decrease in U_{fw} and provides a closer match with the experiment than the uncalibrated case, indicating that the discrepancy observed is at least partly attributable to an incorrect estimate of the absorption coefficient.

4.2. *Three collapse regimes and comparison with experiments*

When collapsing near a rigid wall, the bubble undergoes non-spherical collapse due to the asymmetric pressure gradient imposed by the wall. This pressure gradient leads to

https://doi.org/10.1017/jfm.2026.11781 Published online by Cambridge University Press

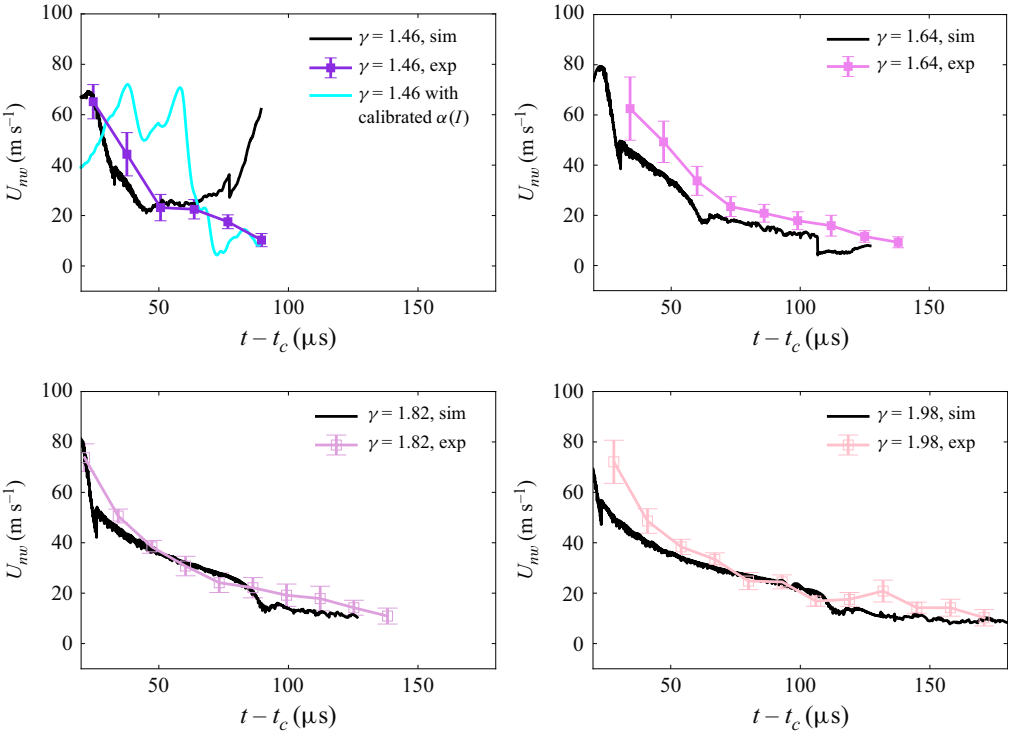


Figure 13. Comparison of the near-wall interface velocity U_{nw}. The absorption coefficient is denoted by $\alpha(I)$.

the emission of multiple spherical pressure waves at distinct instants during the collapse process (Lindau & Lauterborn 2003; Gonzalez-Avila *et al.* 2021). The sources of these pressure waves were systematically categorised by Supponen *et al.* (2017) into three distinct types: jet collapse, tip collapse and torus collapse. More recently, Subramanian *et al.* (2026) experimentally reproduced and validated these three collapse regimes.

In this work we use different terminology to reproduce the three collapse regimes numerically and compare our simulation cases across the range $\gamma \in [0.71, 2.14]$ with the experimental results reported by Subramanian *et al.* (2026). The comparison focuses on two main aspects: the identification of three collapse regimes, and the evolution of the maximum wall pressure $max_r(P_w)$ of the simulated and experimental cases, highlighting three key time instants: (i) the timing of the microjet piercing through the bubble t_j, i.e. the time at which $max(z_{axis})$ and $min(z_{axis})$ are crossing (see figure 11*a*); (ii) the timing of the microjet impacting the wall t_i, defined as the moment when the near-wall interface makes contact with the rigid wall; and (iii) the timing of the pressure peak induced by the first collapse t_p, which occurs very close to the collapse time t_c, defined as the instant when the bubble reaches its volume. Hence, if $t_p \approx t_c$, the pressure peak is primarily associated with the collapse rather than the jet impact, the same conclusion drawn by Yang *et al.* (2025).

Figure 14(*a*) compares the collapse time t_c and the microjet piercing time t_j obtained from the simulations, as well as t_c between experiment and simulation. It is evident that t_c does not generally coincide with t_j. The difference between these two time points reveals the following three distinct collapse regimes observed experimentally by Subramanian *et al.* (2026).

https://doi.org/10.1017/jfm.2026.11781 Published online by Cambridge University Press

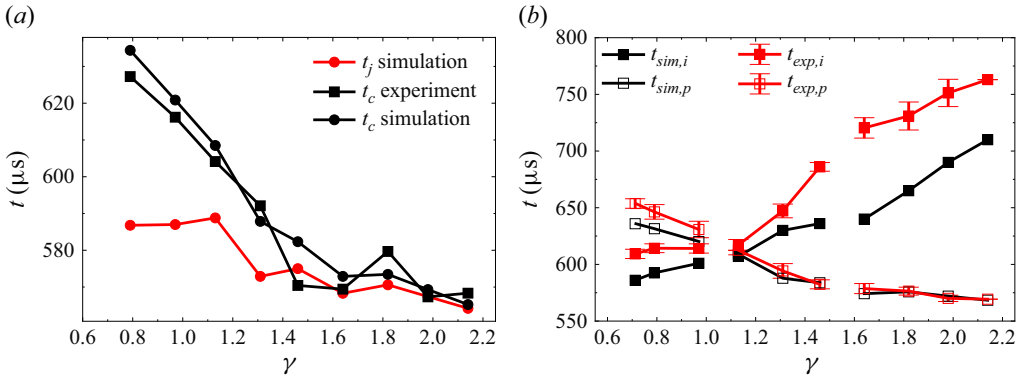


Figure 14. (*a*) Comparison of the bubble collapse time t_c and the microjet piercing through the bubble time t_j from simulations, and comparison between experiment and simulation of t_c. (*b*) Comparison between experiment and simulation of the timing of the microjet impacting the wall t_i and the wall pressure peak time t_p.

(i) $\gamma \leqslant 0.97$: the microjet pierces the bubble significantly earlier than the bubble collapse occurs, i.e. $t_j \ll t_c$, resulting in a purely torus collapse regime (see figure 13 of the experimental study by Subramanian *et al.* 2026).

(ii) $\gamma \in [1.13, 1.46]$: the microjet pierces the bubble shortly before the bubble collapse occurs, with the two time points becoming comparable, i.e. $t_j \simeq t_c$, but yet $t_c > t_j$, leading to a mixed tip-and-torus collapse regime (see figure 14 of the experimental study by Subramanian *et al.* 2026).

(iii) $\gamma \geqslant 1.64$: the microjet pierces the bubble almost concurrently with the collapse of the bubble, i.e. $t_j \simeq t_c$. The collapse is identified as a purely tip collapse regime (see figure 18 of the experimental study by Subramanian *et al.* 2026).

Furthermore, we observe a very good agreement between the experiment and simulations in terms of t_c, which reinforces the validity of the three regimes identified through the simulation. From figure 14(*b*) it is evident that both the simulation and experimental results show the same trend in terms of both the microjet impact time on the wall t_i and the occurrence of the pressure peak at the wall t_p, while noticeable discrepancies exist between $t_{sim,i}$ and $t_{exp,i}$, indicating that the experimentally observed microjet propagates more slowly than in the numerical model. The discrepancy is attributed to physical effects not included in the present inviscid model, such as viscous dissipation and near-wall boundary-layer effects, which accumulate with γ as the jet travels a longer distance before reaching the wall, until a sufficiently large γ, i.e. $\gamma = 1.64$, is reached. In addition, the experimental definition of impact time based on optical detectability can introduce a timing uncertainty of at least 13 μs, given the frame interval of the high-speed imaging.

In the following sections a detailed comparison between simulations and experiments will be carried out for each of the three collapse regimes, analysed individually. To establish confidence in the numerical model, we begin with the first and third collapse regimes, as they are easier to reproduce since they rely on a single collapse mechanism, either torus or tip collapse. The second regime, where tip-and-torus collapse interact, is presented last and analysed in greater detail.

4.2.1. *Torus collapse regime*

In the torus regime, where the bubble is initially located close to the wall ($\gamma \leqslant 0.97$), the bubble exhibits a purely torus collapse as shown in figure 15. The microjet pierces

https://doi.org/10.1017/jfm.2026.11781 Published online by Cambridge University Press

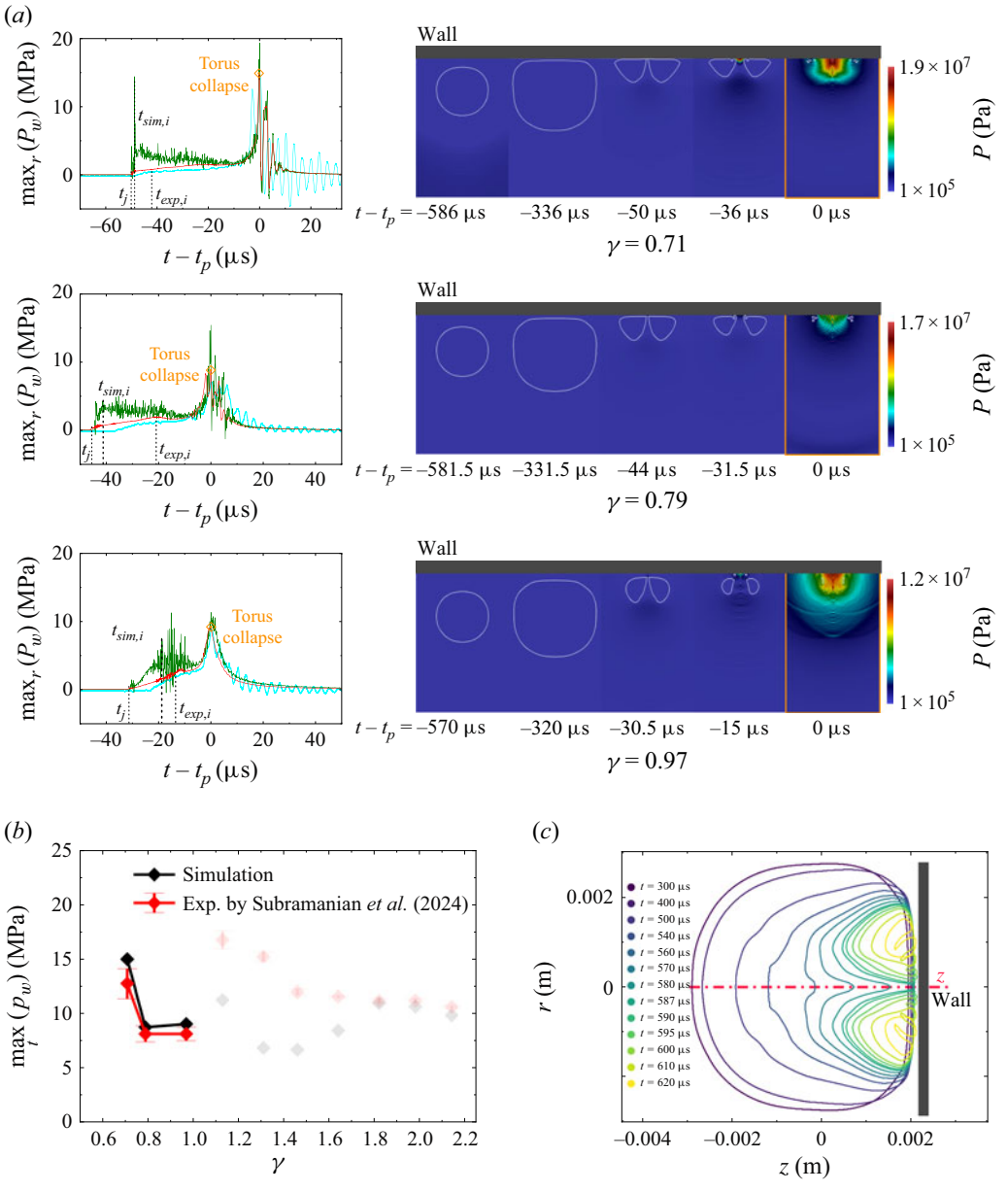


Figure 15. Torus collapse regime for $\gamma \in [0.79, 0.97]$: (*a*) temporal evolution of wall pressure from simulation: pressure at wall centre (green), pressure averaged over the sensor area (red), and experimental measurements (cyan) (left panels) and bubble topology visualisation with the pressure field at key moments (right panels). The timing of the near-wall interface hitting the wall is denoted by t_i, where $t_{sim.,impact}$ is for the simulations and $t_{exp.,impact}$ is for the experiments. (*b*) Comparison between experiments and simulations in the maximum pressure at the wall. (*c*) Toroidal contour evolution for $\gamma = 0.79$.

through the near-wall interface of the bubble significantly before the bubble reaches its minimum volume as shown in figure 14(*a*), defining the feature of the first collapse regime described by Subramanian *et al.* (2026), where the bubble undergoes a purely toroidal collapse. Immediately after the piercing time t_j, due to the combined effect of the microjet impingement and the close proximity to the wall, the collapse is hindered, i.e. the bubble

https://doi.org/10.1017/jfm.2026.11781 Published online by Cambridge University Press

volume decreases more slowly. This combined effect promotes radial spreading of the bubble interface while limiting the axial propagation. The near-wall interface begins to roll up into a toroidal shape starting from t_j and continues until the end of the first rebound, as shown in figure 15(*c*).

There is strong agreement between the simulations and the experimental cases in terms of wall pressure evolution, peak wall pressure over γ and bubble collapse time. Three distinct time points are identified as shown in figure 15(*a*): the piercing time t_j, the jet impact time t_i and the maximum wall pressure time t_p, respectively. Right after t_j, the pressure wave is emitted and a pressure rise is observed. This pressure wave propagates faster than the jet itself and reaches the wall earlier, producing a localised pressure rise prior to the actual jet impact at t_i. Importantly, the deviation in both t_i and t_p between simulation and experiment remains below 5 %, as also shown in figure 14(*b*), confirming the accuracy and consistency of the simulation in capturing the bubble dynamics. Moving from $\gamma = 0.71$ to $\gamma = 0.97$, the time difference between t_j and t_p decreases from 49 µs to 20 µs in the simulations and from 42 µs to 15 µs in the experiments, indicating that the two events become increasingly close in time within this regime. Moreover, with increasing γ, the time required for the microjet to impact the wall t_i increases due to the increased bubble–wall distance, whereas the time to reach peak wall pressure t_p decreases, consistent with the observed trend in bubble collapse time t_c resulting from reduced wall confinement.

Noticeable oscillatory behaviour and negative values are observed in the pressure at the wall centre (see green curves in the left panels of figure 15*a*) within this regime. After jet piercing of the near-wall interface, strong pressure waves are emitted. These waves reach the wall rapidly, reflect toward the bubble and undergo multiple reflections between the bubble interface and the wall. The oscillations are therefore a consequence of the propagation and reflection of the pressure wave, especially for the bubble close to the wall. The absence of similar violent oscillations in the other two regimes further supports this explanation. Moreover, the pressure at the wall centre corresponds to the pressure localised at a single computational grid point, which makes it highly sensitive to pressure waves. To obtain a more comparable prediction, the pressure is also averaged over a pressure sensor area of 1 mm radius along the wall, consistent with the experimental configuration (see red curves in the left panels of figure 15*a*). This spatial averaging yields a much more robust pressure prediction compared with the measurement at the wall centre. We stress that the appearance of negative pressure values is physically normal and expected as stiffened gas equations of state are designed to allow negative pressure in the liquid phase (i.e. tension), as stated in § 2.2.

Regarding the bubble collapse time depicted in figure 14(*a*), both simulation and experiment demonstrate a consistent trend: the bubble collapses earlier as γ increases. The collapse time t_c predicted by the simulation is closely aligned with the experimental measurements, reinforcing a strong agreement between the two. The consistency of this regime is further reflected in figure 15(*b*), in which the maximum wall pressure is observed to decrease with increasing γ.

4.2.2. *Tip collapse regime*

When the bubble is located sufficiently far from the wall, that is, for $\gamma \geqslant 1.64$, a tip collapse regime is observed (see figure 16). Within this regime, the microjet pierces through the bubble almost simultaneously with the bubble collapse, i.e. $|t_p - t_j| \leqslant 4$ µs (see the right panels of figure 16*a*), indicating a quasi-simultaneous occurrence of the piercing and collapse events. Due to the reduced influence of the wall, once the near-wall

https://doi.org/10.1017/jfm.2026.11781 Published online by Cambridge University Press

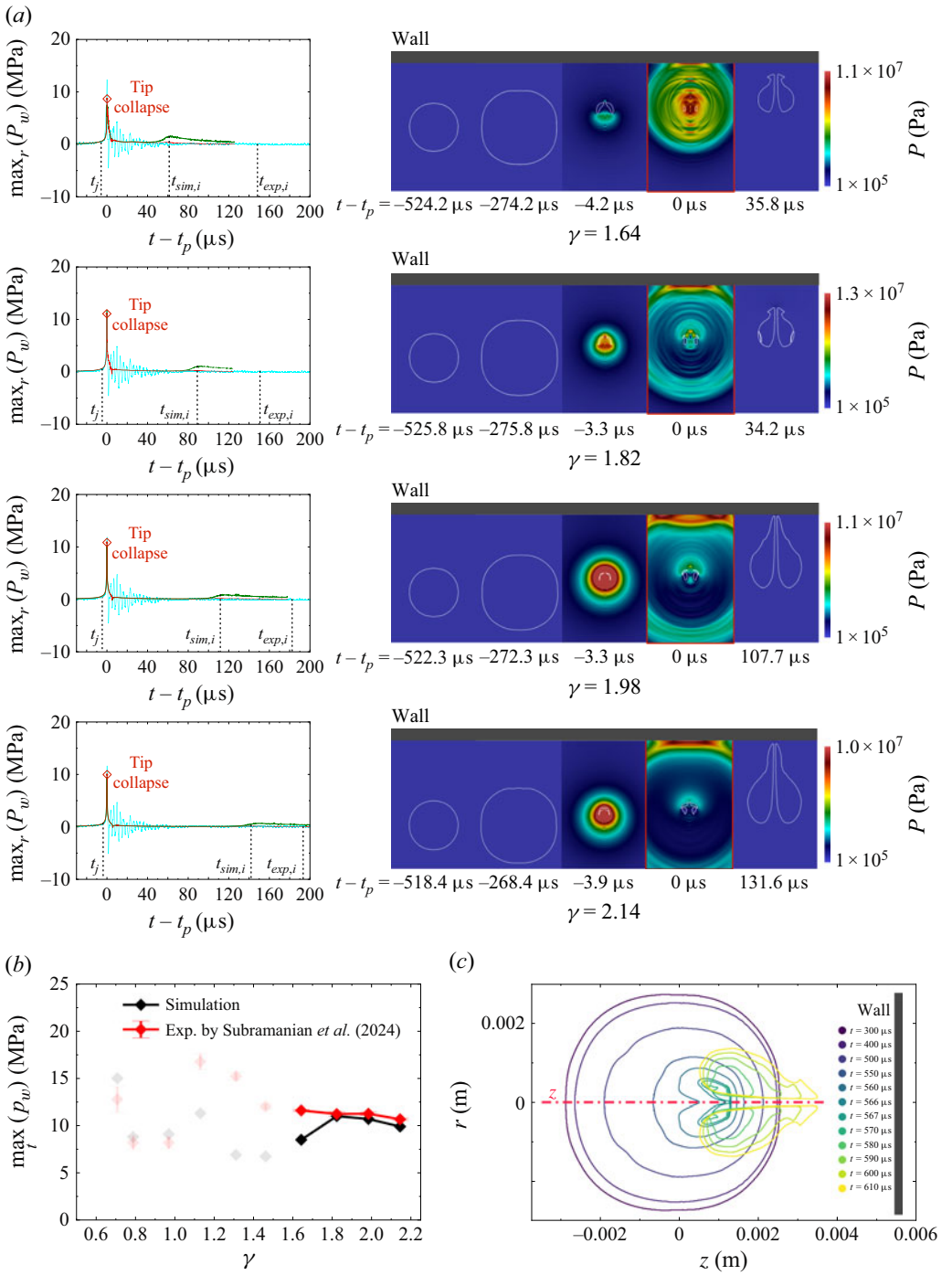


Figure 16. Tip collapse regime for $\gamma \in [1.64, 2.14]$: (*a*) temporal evolution of wall pressure from simulation: pressure at wall centre (green), pressure averaged over the sensor area (red), and experimental measurements (cyan) (left panels) and bubble topology visualisation with the pressure field at key moments (right panels). The timing of the near-wall interface hitting the wall is denoted by t_i, where $t_{sim.,impact}$ is for the simulations and $t_{exp.,impact}$ is for the experiments. (*b*) Comparison between experiments and simulations in the maximum pressure at the wall. (*c*) Tip contour evolution for $\gamma = 1.98$.

https://doi.org/10.1017/jfm.2026.11781 Published online by Cambridge University Press

interface of the bubble is pierced by the microjet, the tip of the bubble interface is advected by the flow towards the wall. The bubble interface spreads much faster in the axial directions than in the radial direction.

Three distinct time points are again identified: the piercing time t_j, the microjet impact time t_i and the maximum wall pressure time t_p, respectively. As γ increases, the time required for the microjet to impact the wall increases dramatically. Simulations indicate that the delay between the bubble collapse and jet impact grows from around 60 µs at $\gamma = 1.64$ to about 140 µs at $\gamma = 2.14$, while in experiments, this gap extends from approximately 149 µs to over 200 µs as shown in the left panels of figure 16(*a*). This trend confirms that the bubble collapse event dominates the bubble dynamics, and the microjet arrives too late to contribute meaningfully to the observed pressure peak. Although the near-wall interface eventually contacts the wall, it generates only a minor localised pressure rise at t_i, which is generally undetectable in experiments due to the sensor limitation. No distinct pressure rise from the jet impact is therefore recorded in the experimental data.

The maximum wall pressure, presented in figure 16(*b*), further validates the tip collapse regime as identified by Subramanian *et al.* (2026). The simulation results show strong overall agreement with the experimental data, confirming a plateau of approximately 10 MPa for $\gamma \gtrsim 1.82$. A mismatch is observed specifically at $\gamma = 1.64$, which we hypothesise is due to the high sensitivity of the model to the absorption coefficient near the regime boundary, as further analysed in § 4.2.3.1.

4.2.3. *Mixed tip-and-torus collapse regime*

The mixed tip-and-torus collapse regime identified for $\gamma \in [1.13, 1.46]$ and depicted in figure 17 is the most intricate dynamics among the cases we consider. Within this regime, the bubble piercing time t_j is comparable to but still appreciably larger than the bubble collapse time t_c. As the stand-off ratio γ increases, the collapse phase is characterised by a tip collapse triggered shortly after the microjet pierces the near-wall interface of the bubble. At this stage, the bubble still resides at a moderate distance from the wall (see the right panels of figure 17*a*). The pressure difference between the near-wall and far-wall interfaces induces a net translational motion of the bubble toward the wall, advecting the jet tip along with it. Consequently, the early collapse proceeds predominantly in the axial direction, with the interface collapsing faster toward the wall than radially. This defines a first tip collapse dynamics. However, as the microjet approaches the wall, the proximity to the boundary fundamentally alters the dynamics of the collapse. Axial motion becomes increasingly constrained by the wall, while radial expansion is amplified. The near-wall interface begins to roll up, initiating a torus collapse dynamics, as shown in figure 17(*c*). The resulting interaction between tip-and-torus collapse mechanisms leads to energy redistribution, particularly through wave refraction and dissipation before reaching the wall. As a result, the maximum pressure at the wall is decreased passing from $\gamma = 1.13$ to $\gamma = 1.46$. This dynamic sequence gives rise to a mixed tip-and-torus collapse regime, as confirmed in figure 14(*a*), where both mechanisms interact temporally and spatially.

While it presents a obvious discrepancy in figure 17(*b*) between simulation and experimental results in the prediction of the pressure at the wall, we have a good agreement with the experimental measurements regarding the prediction of t_c in figure 14(*a*), as well as t_i and t_p in figure 14(*b*). We speculate that the pressure discrepancy arises from a high sensitivity of the maximum wall pressure to the fast interfacial dynamics, partially controlled by the sensitivity to the initial growth dynamics and, hence, to the absorption coefficient. Additional sensitivity tests performed in the purely tip and purely

https://doi.org/10.1017/jfm.2026.11781 Published online by Cambridge University Press

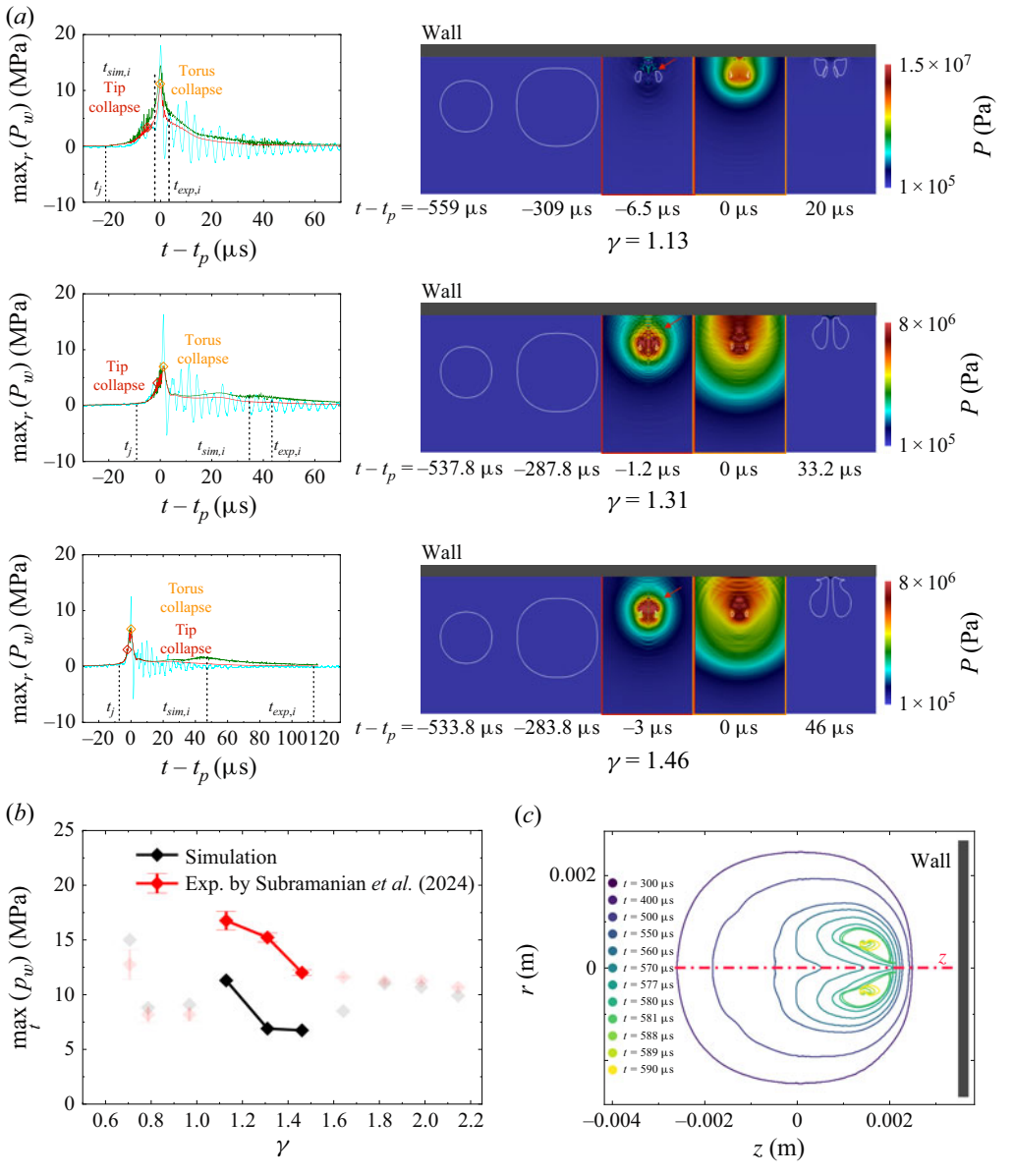


Figure 17. Mixed tip-and-torus collapse regime for $\gamma \in [1.13, 1.46]$: (*a*) temporal evolution of wall pressure from simulation: pressure at wall centre (green), pressure averaged over the sensor area (red), and experimental measurements (cyan) (left panels) and bubble topology visualisation with the pressure field at key moments (right panels). The timing of the near-wall interface hitting the wall is denoted by t_i, where $t_{sim.,impact}$ is for the simulations and $t_{exp.,impact}$ is for the experiments. (*b*) Comparison between experiments and simulations in the maximum pressure at the wall. (*c*) Mixed tip-and-torus contour evolution for $\gamma = 1.31$.

torus collapse regimes show no significant qualitative or quantitative changes when varying the absorption coefficient within a reasonable range. Besides, the repeatability for the mixed torus-and-tip collapse regime by multiple experiments with the same experimental apparatus is even harder to achieve, compared with the other two regimes (see Appendix E). This indicates that the strong sensitivity to the absorption coefficient is

https://doi.org/10.1017/jfm.2026.11781 Published online by Cambridge University Press

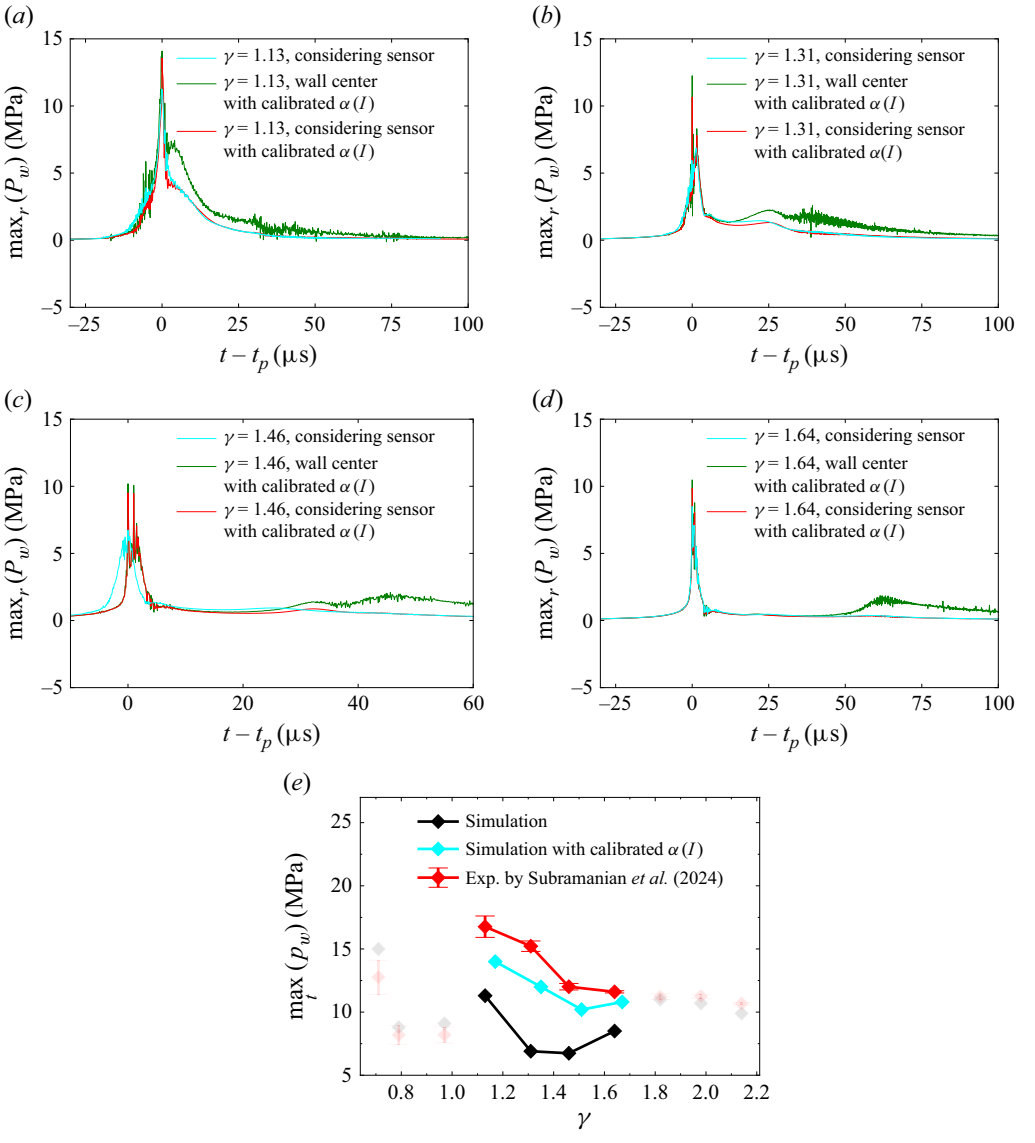


Figure 18. Analysis of sensitivity to the absorption coefficient: temporal evolution of wall pressure from simulation with calibrated absorption coefficient for (*a*) $\gamma = 1.13$, (*b*) $\gamma = 1.31$, (*c*) $\gamma = 1.46$, and (*d*) $\gamma = 1.64$. (*e*) Comparison between experiments and simulations in the maximum pressure at the wall. The absorption coefficient is denoted by $\alpha(I)$.

specific to the mixed regime. The following section presents a detailed parameter study to quantify this relationship and validate our hypothesis.

4.2.3.1. Sensitivity to absorption coefficient We investigate the sensitivity of bubble dynamics, particularly the peak wall pressure during the mixed tip-and-torus collapse regime, to the absorption coefficient. Figure 18 presents the maximum wall pressure obtained from four new simulations with adjusted absorption coefficient: $\gamma = 1.13$ with the absorption coefficient of $75\,000\,\mathrm{m}^{-1}$, $\gamma = 1.31$ with $73\,000\,\mathrm{m}^{-1}$, $\gamma = 1.46$ with $71\,400\,\mathrm{m}^{-1}$ and $\gamma = 1.64$ with $80\,000\,\mathrm{m}^{-1}$, as reported in table 2. The selected absorption coefficients result from a simulation campaign of a systematic parametric study in which

https://doi.org/10.1017/jfm.2026.11781 Published online by Cambridge University Press

γ	$\alpha(I)$ (m^{-1})	$\max_t(R_{eq})$ (mm)	$\max_{t,r}(P_w)$ (MPa)	P_L/P_G $t=t(R_{max})$	t_c (μs)	t_c^*	$\max_{t,r}(P_w)^*$	$\max_t(T_{avg})$ (K)	$\max_t(T_{avg})^*$
0.79	100 000	2.69	8.8	54.9	634.4	2.35	88.5	837.8	2.86
0.97	100 000	2.72	9.1	54.2	620.9	2.28	91.5	1541.8	5.26
1.13	75 000	2.64	14.0	60.0	578.0	2.19	140.5	1813.6	6.19
1.31	73 000	2.67	12.0	63.5	567.0	2.12	120.3	2078.1	7.09
1.46	71 400	2.58	10.2	65.0	544.0	2.11	102.2	2213.8	7.55
1.64	80 000	2.65	10.8	64.0	552.1	2.08	108.3	2454.7	8.37
1.82	100 000	2.78	11.0	55.9	573.5	2.06	110.5	3023.9	10.31
1.98	100 000	2.78	10.7	55.9	569.3	2.04	107.5	3227.9	11.01
2.14	100 000	2.79	9.9	61.0	565.3	2.02	99.3	3596.6	12.27

Table 2. Input parameters and key quantities for different γ. Three non-dimensional parameters, i.e. t_c^*, $\max_{t,r}(P_w)^*$ and $\max_t(T_{avg})^*$ are scaled by $\max_t(R_{eq})\sqrt{\rho_0/\Delta p}$, Δp and T_0, respectively, where $\Delta p = P_L - P_G$, P_L and P_G are the liquid water and water vapour pressure at $t = t(R_{max})$.

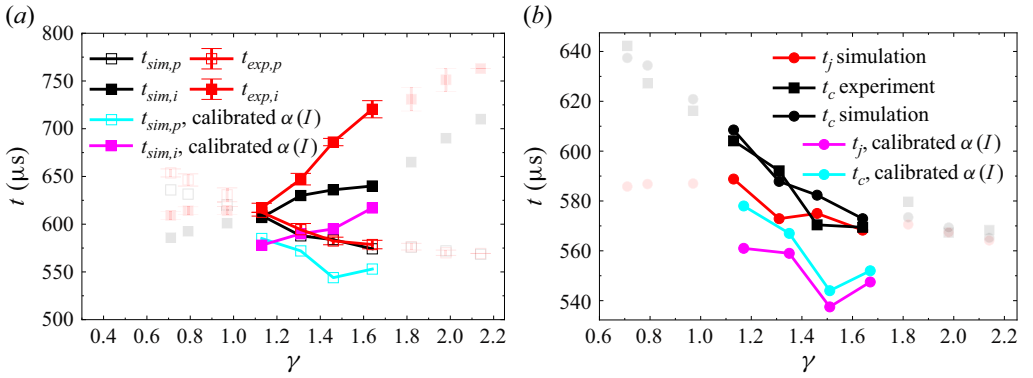


Figure 19. Sensitivity to the absorption coefficient: (*a*) time of the microjet impacting the wall compared with the pressure peak time of first collapse. Here t_i refers to the timing of the microjet hitting the wall. (*b*) Comparison of the bubble collapse time t_c and the microjet piercing through the bubble time t_j from simulations, and of the collapse time t_c between experiment and simulation. The absorption coefficient is denoted by $\alpha(I)$.

a range of values was explored to assess the influence on wall pressure prediction. The reported values correspond to those that minimise the discrepancy between simulations and experiments in terms of pressure peak at the wall. As a result, the optimised absorption coefficients bring the simulated peak wall pressure significantly closer to the experimental measurements (see figure 18*e*). Although this modification leads to certain deviation in the timing characteristics, specifically the microjet impact time t_i, pressure peak time t_p in figure 19(*a*), piercing time t_j and collapse time t_c in figure 19(*b*), the overall gain in pressure prediction accuracy justifies the trade-off. The relative error in peak wall pressure decreased substantially, from an initial range of 30 %–60 % to a much improved 4 %–15 % of relative error over the range $\gamma \in [1.13, 1.64]$. In contrast, the maximum relative errors in key temporal parameters increased slightly: t_i passed from 5 % to 14 %, t_p from 4 % to 7 %, t_j to 7 % and t_c from 2 % to 5 %.

Although there is a modest reduction in the accuracy of temporal predictions, the significant improvement in pressure prediction by a factor of over 4 represents a favourable trade-off of the bubble generation model parameters, especially considering the

https://doi.org/10.1017/jfm.2026.11781 Published online by Cambridge University Press

importance of pressure in assessing cavitation-induced damage. This sensitivity analysis with respect to the absorption coefficient indirectly demonstrates the capacity of our model in reproducing cavitation bubble dynamics observed in experiments; however, it stresses that an accurate reproducibility of the second collapse regime might be hard to achieve. This is also confirmed experimentally comparing the experimental measurements reported in Yang *et al.* (2025) and Subramanian *et al.* (2026), as a change in composition or ionisation of the water would be expected to have a significant impact on the bubble nucleation. This analysis suggests that this is especially the case for the mixed tip-and-torus regime pointing towards the absorption coefficient as one of the leading-order effects.

4.3. *Cavitation bubble dynamics for different stand-off ratios*

Having validated the robustness of the computational model through detailed comparison with experiments, we now numerically examine the cavitation bubble dynamics for three selected stand-off ratios, $\gamma = 0.97$, 1.64 and 2.14, focusing on the temporal evolution of key physical fields, including velocity, pressure and temperature fields, as well as the liquid–gas interface (shown in magenta). The streamlines indicating the direction of flow are also shown (white lines and arrows). These cases provide insights into how the increase of γ influences the bubble dynamics and thermal evolution. The absorption coefficient used for these simulations are reported in table 2.

4.3.1. *Pressure dynamics*

Initially, all three cases behave similarly, characterised by a sharp increase in bubble spatially averaged pressure to over 220 MPa immediately after bubble formation, as observed in figure 20, corresponding to a pressure ratio of $P_G/P_L \approx 2000$, where $P_G = (1/V_b)\int_{V_b} p(z, r)\,\mathrm{d}V$. The pressure at (z, r) inside the bubble is denoted by $p(z, r)$ and V_b is the volume of the bubble. The large pressure difference drives the rapid initial expansion of the bubble. This high initial pressure results from the extremely high internal temperature generated by the absorption of laser energy. As shown in figure 23(*a*) for the case $\gamma = 0.97$, the initial temperature reaches approximately 23 000 K. A comparably high temperature is observed for $\gamma = 2.14$ in figure 24(*a*). For $\gamma = 1.64$, the initial temperature is slightly lower ($\sim$20 000 K) due to the lower absorption coefficient (see figure 25*a*). The internal energy dissipates as the bubble grows, causing the gas pressure to decrease throughout the expansion phase. When the bubble reaches its maximum size $\max_t(R_{eq})$, the gas pressure stabilises at a remarkably consistent magnitude across all cases until the end of the first rebound (see the right panels of each case in figure 20 and table 2). At $\max_t(R_{eq})$, the pressure ratio P_L/P_G falls within the range [54, 65], initiating the bubble collapse. Notably, the gas pressure for $\gamma = 1.64$ is consistently lower compared with the other two cases. We stress that this difference stems from a smaller absorption coefficient, which was calibrated to better reproduce the wall pressure measured from the experiment by Subramanian *et al.* (2026).

The huge initial bubble pressure drives the rapid initial expansion of the bubble with a significant momentum increase. The key stages of subsequent bubble dynamics, including pressure and velocity field for the three cases, are presented in figure 21. Each snapshot presents the velocity field (upper half) and pressure field (lower half), along with the direction of flow at each depicted moment. While the pressure inside the bubble drops as the gas phase works against the surrounding fluid, the effect of accumulated inertia initially allows the bubble to continue to grow to its maximum size (at around $t - t_c = -312$ μs) at which the pressure within the bubble becomes nearly uniform. At this moment,

https://doi.org/10.1017/jfm.2026.11781 Published online by Cambridge University Press

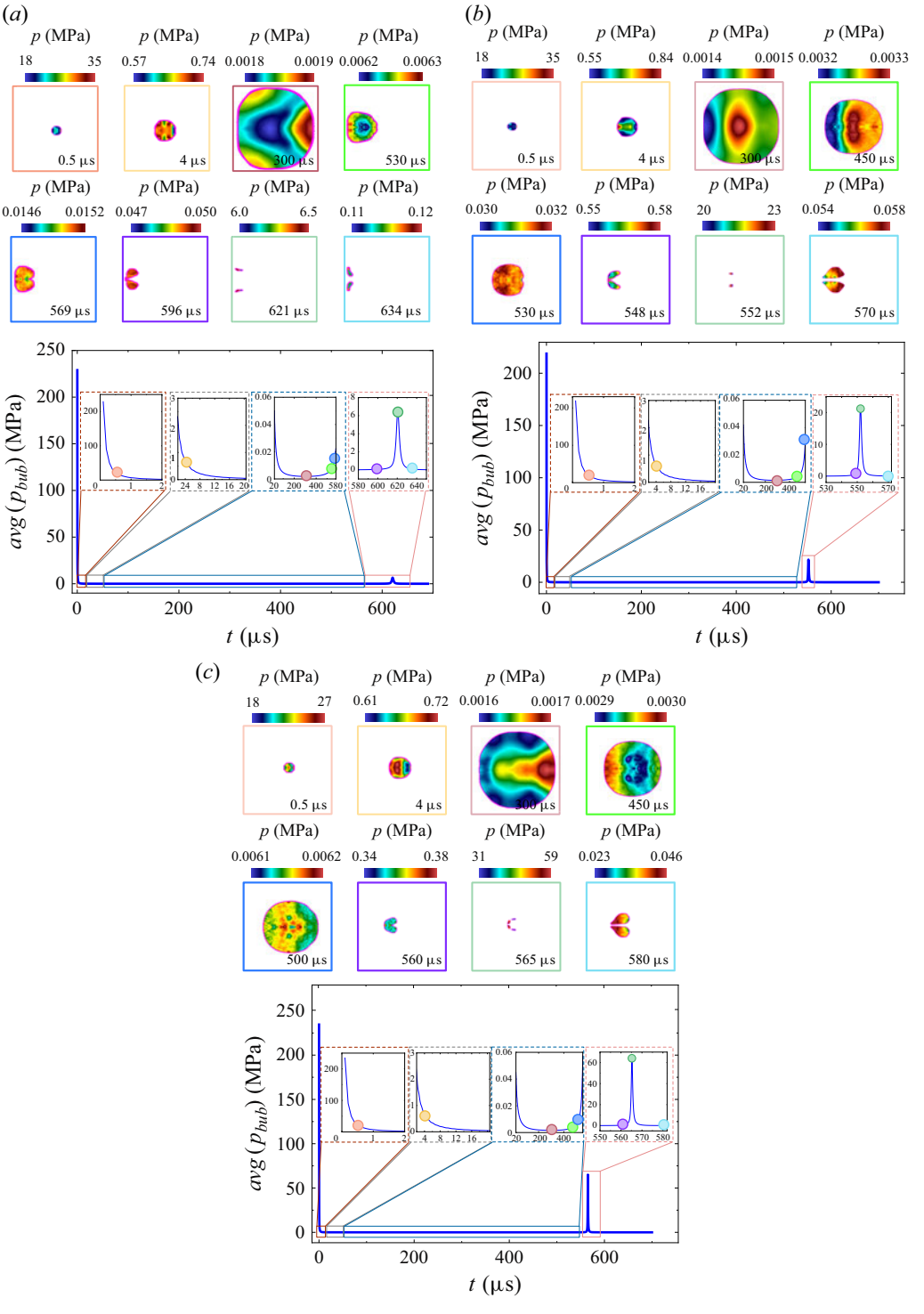


Figure 20. Temporal evolution of the average pressure inside the bubble $avg(P_{bub})$ with the snapshots of the pressure fields at different times for stand-off ratios (*a*) $\gamma = 0.97$, (*b*) $\gamma = 1.64$, (*c*) $\gamma = 2.14$. The collapse time is denoted as t_c and equals $t_c = 620.9$ μs for $\gamma = 0.97$, $t_c = 552.1$ μs for $\gamma = 1.64$, $t_c = 565.3$ μs for $\gamma = 2.14$. Particularly, four snapshots on the side are further picked at the time approaching collapse.

https://doi.org/10.1017/jfm.2026.11781 Published online by Cambridge University Press

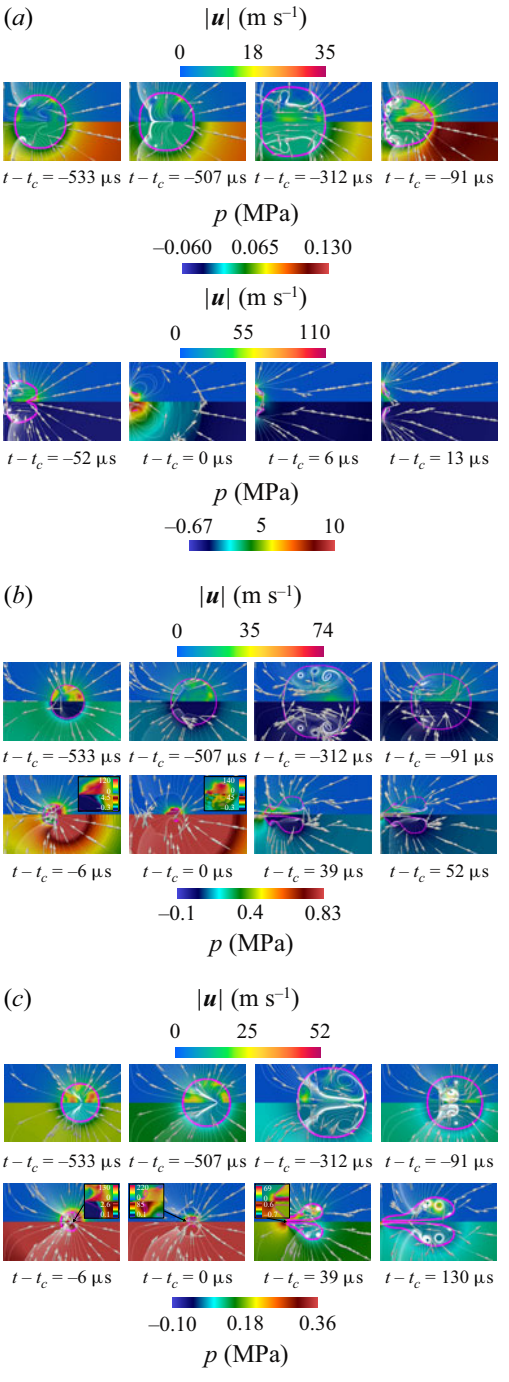


Figure 21. Snapshots of the velocity field (upper half) and pressure field (lower half) at different times for stand-off ratios (*a*) $\gamma = 0.97$, (*b*) $\gamma = 1.64$, (*c*) $\gamma = 2.14$. The collapse time is denoted as t_c and equals $t_c = 620.9\ \mu s$ for $\gamma = 0.97$, $t_c = 552.1\ \mu s$ for $\gamma = 1.64$, $t_c = 565.3\ \mu s$ for $\gamma = 2.14$. The wall is aligned with the left boundary in each subfigure.

https://doi.org/10.1017/jfm.2026.11781 Published online by Cambridge University Press

velocity gradients still exist across the gas–liquid interface, giving rise to vorticity within the bubble even in the absence of viscosity. The toroidal vortex attached to the interface inside the bubble can be observed in figure 21, becoming particularly more evident for larger γ where the weaker wall effect allows the bubble to expand more isotropically, enabling a more fully developed and symmetric vortex ring to form. This vorticity induced by the velocity difference establishes a coherent toroidal recirculation within the bubble and organises the internal flow structure for the subsequent collapse dynamics.

After the bubble reaches its maximum size, the surrounding pressure becomes dominant (see figure 21). The flow direction reverses, pointing towards the bubble as it enters the collapse phase ($t - t_c = -312$–$0\,\mu$s). High pressure and velocity are concentrated in the normal direction towards the wall, particularly near the far-wall interface of the bubble. This results in intense compression and the subsequent emission of a strong pressure signal at collapse. At collapse time, i.e. $t - t_c = 0\,\mu$s, the maximum velocity in the fluid coincides with the emission of a pressure wave, which corresponds to the second pressure peak in the surrounding liquid. The intensity of this peak and the associated temperature peak vary significantly with the stand-off ratio. The pressure rises to 10 MPa and the temperature to 1738 K for $\gamma = 0.97$, to approximately 40 MPa and 2593 K for $\gamma = 1.64$, and to 85 MPa and 4222 K for $\gamma = 2.14$. This trend is clearly visible in the temporal evolution of the temperature field for $\gamma = 0.97$ (figure 23*a*), which shows a low amplitude peak. The progressively higher peaks for the other cases are detailed in figures 24(*a*) and 25(*a*). More details of bubble dynamics at t_c are reported in Appendix B. Following the collapse, the flow direction reverses once again, pointing away from the bubble as it enters the rebound phase. The pressure field relaxes rapidly as the bubble expands again.

4.3.2. *Interfacial dynamics*

Right after the bubble forms, the high gas pressure drives nearly symmetric bubble expansion in all directions. In fact, for $t < 150\,\mu$s, the bubble expands, i.e. the increase of equivalent radius R_{eq} (figure 22*a*), simultaneously in the radial and axial direction with nearly the same speed of growth, and the far-wall and near-wall interfaces of the bubble also expand at almost the same speed (see figure 22*b–d*). But during the late expansion phase for $150\,\mu\text{s} < t < 300\,\mu$s, for the smallest stand-off ratio, the wall effect is maximal, restricting the expansion to the axial direction. Thus, the increases of the bubble volume are mainly due to the increases of the radial dimension of the bubble for $\gamma = 0.97$ (see $max(D_s)$, where 's' denotes the bubble surface; blue line in figure 22*d*), rather than of its axial dimension (see $max(\Delta z_s)$; blue line in figure 22*c*).

During the early phase of collapse for $300\,\mu\text{s} < t < 500\,\mu$s, the collapse of the bubble is dominated by a radial compression. Once the cavitation bubble reaches an oblong shape, the radial component of the pressure gradient inside the bubble becomes significantly larger than the axial one, accelerating axial compression due to the presence of the wall and leading eventually to the formation of a dimple on the far-wall interface of the bubble (see $t - t_c = -52\,\mu$s for $\gamma = 0.97$ and $t - t_c = -6\,\mu$s for $\gamma = 1.64$ and 2.14 in figure 21). This asymmetry pushes the far-wall interface towards the wall faster than the near-wall interface (see $t > 500\,\mu$s in figure 22*b*). As a result, the bubble centroid moves towards the wall while the bubble is shrinking, as explained in § 4.1.

Meanwhile, a microjet is forming and subsequently piercing the near-wall interface of the bubble. As γ increases, the velocity of this microjet also increases from about 35 m s^{-1} to 130 m s^{-1} on its way to the solid wall (see $t - t_c = -91\,\mu$s for $\gamma = 0.97$ and $-6\,\mu$s for 1.64 and 2.14 in the velocity diagram series). At $t - t_c = 0\ \mu$s, the maximum velocity in

https://doi.org/10.1017/jfm.2026.11781 Published online by Cambridge University Press

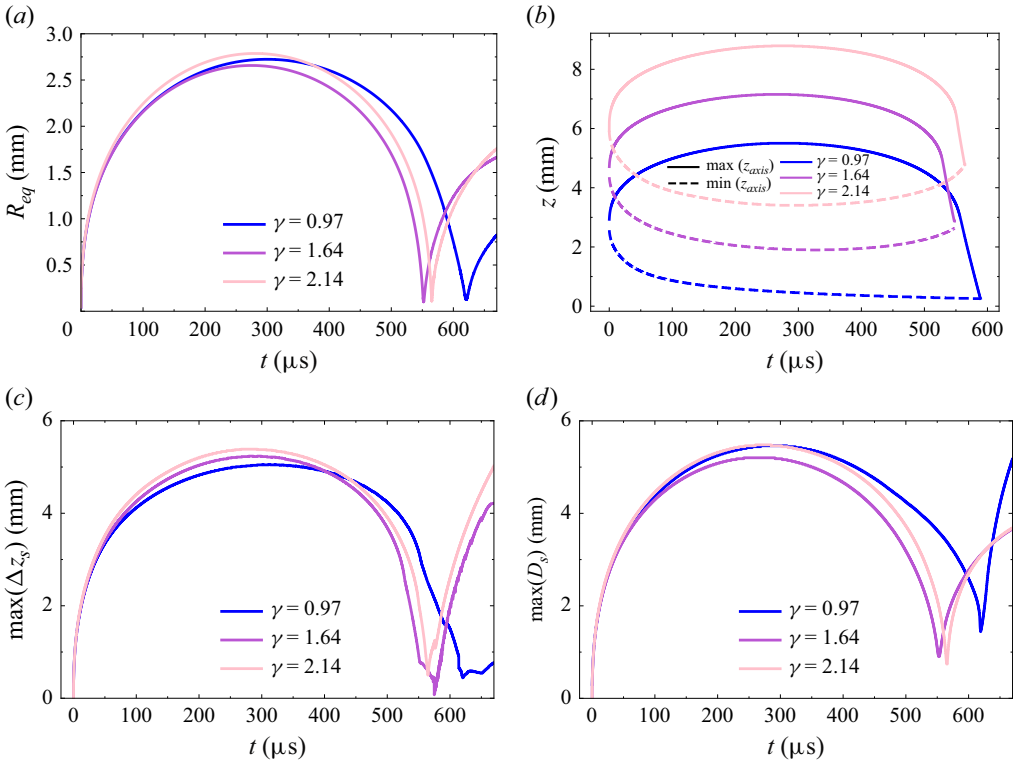


Figure 22. (*a*) Temporal evolution of the equivalent radius R_{eq}. (*b*) Minimum and maximum positions of the bubble interface on the z axis. Maximum length of the bubble in the (*c*) axial $max(\Delta z_s)$ and (*d*) radial $max(D_s)$ directions, where 's' denotes the bubble surface. For $\gamma = 1.64$, the absorption coefficient is relatively small, at 80 000 m^{-1}.

the fluid, ranging from 110 $\mathrm{m\,s}^{-1}$ for $\gamma = 0.97$ to 220 $\mathrm{m\,s}^{-1}$ for $\gamma = 2.14$ is observed. In this phase, the jet extends up to the solid wall in all cases. It is noticeable that the time required for the microjet to impact on the wall increases with γ. The maximum velocity is observed at the tip of the jet near the solid wall but continuously decreases as the jet advances through the liquid.

4.3.3. *Temperature dynamics*

Contrary to internal pressure, the temperature inside the bubble for all γ is not quasi-uniformly distributed, as shown in figures 23(*a*)–25(*a*). It is observed that throughout the bubble lifetime, the centroid progressively shifts toward the wall, and correspondingly, the hottest region also migrates closer to the wall. At the early moment, the temperature field inherits the initial nearly spherical symmetry, centred around a localised hot spot as the laser focus is aligned with the centroid of the bubble. This leads to radially driven hot fingers (see the earliest two snapshots in figures 23*a*–25*a*), which can be attributed to the advection of heat within the vapour phase. The fluid motion inside the bubble driven by pressure gradients and flow direction redistributes the heat unevenly, as also understood by examining the streamlines at $t - t_c = -533$ μs and -507 μs in figure 21. The advection of hot vapour outward from the centre, combined with variations in flow velocity, causes the temperature field to elongate and branch out along preferential directions, giving rise to a 'star-like' temperature pattern.

https://doi.org/10.1017/jfm.2026.11781 Published online by Cambridge University Press

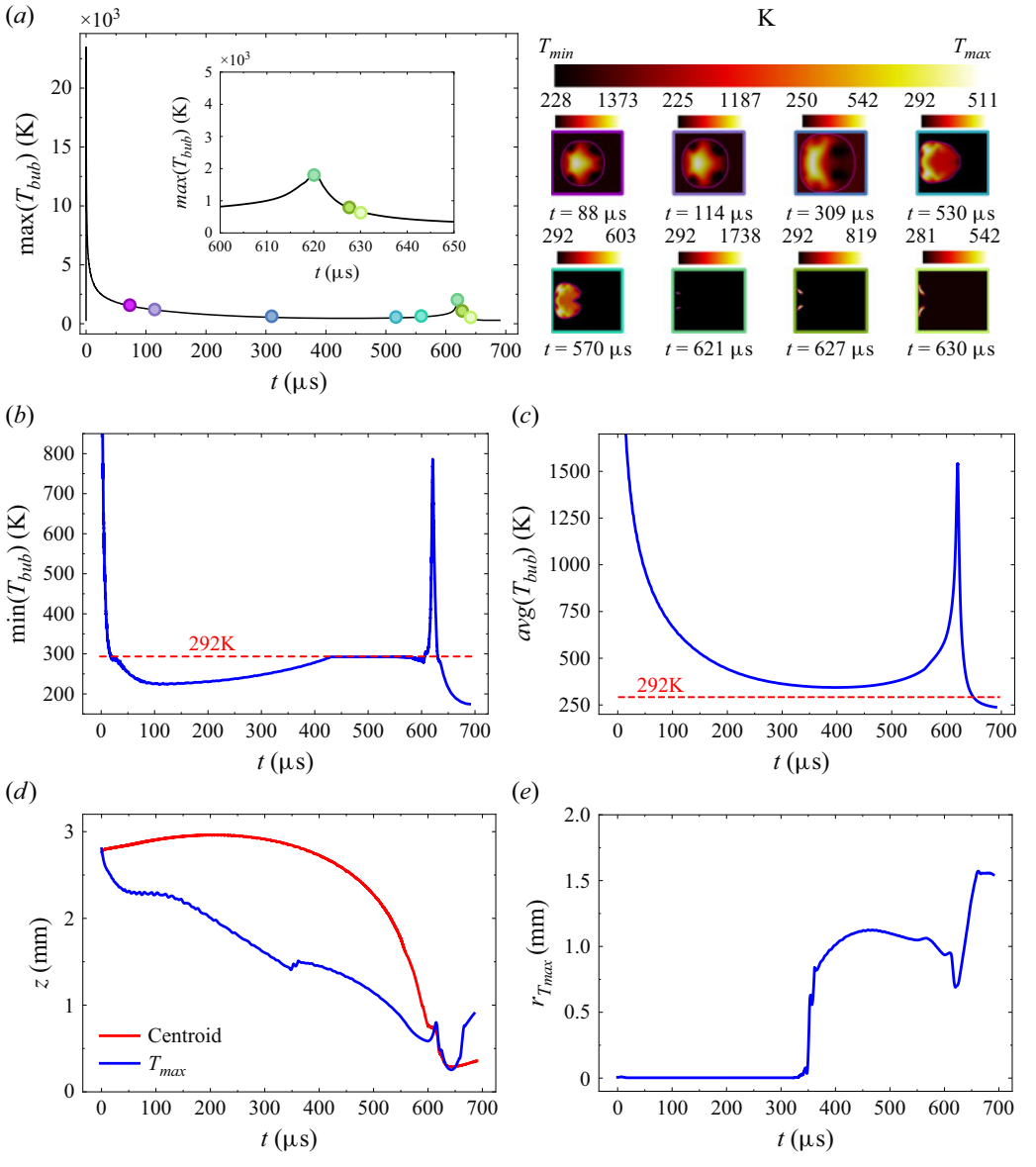


Figure 23. Temperature profile for $\gamma = 0.97$. (*a*) Maximum temperature evolution over time with the snapshots of the temperature fields at different times. The wall is aligned with the left boundary in each subfigure. The inset image represents the zoom-in of the maximum temperature evolution near bubble collapse. Minimum (*b*) and average (*c*) temperature evolution over time with the reference temperature of 292 K. (*d*) Comparisons of the distance to the wall from the bubble centroid and the location of maximum temperature. (*e*) Temporal evolution of distance from the maximum temperature location to the z axis. The collapse time is denoted by t_c and equals $t_c = 620.9$ μs.

As the bubble grows, the symmetry of this star-like pattern begins to break due to the presence of the wall. At later times (see the third to fifth snapshots in figures 23*a*–25*a*), the temperature field evolves into a quasi-symmetric 'pillow-like' shape, with the high-temperature region displaced toward the wall. This transformation can be explained by the continued advection of hot vapour along evolving flow paths inside the bubble and

https://doi.org/10.1017/jfm.2026.11781 Published online by Cambridge University Press

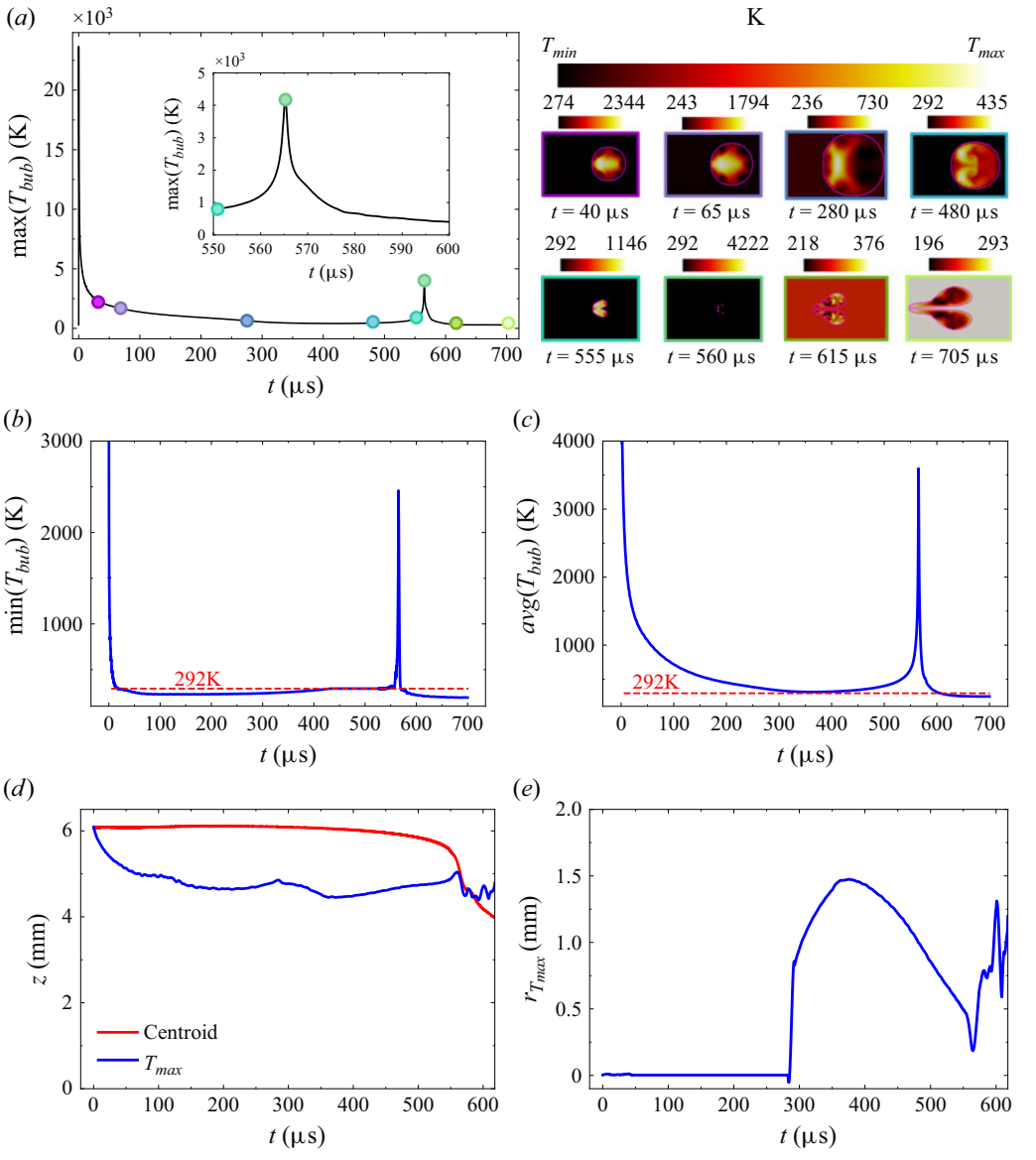


Figure 24. Temperature profile for $\gamma = 2.14$. (*a*) Maximum temperature evolution over time with the snapshots of the temperature fields at different times. The wall is aligned with the left boundary in each subfigure. The inset image represents the zoom-in of the maximum temperature evolution near bubble collapse. (*b*) Minimum temperature evolution over time with the reference temperature of 292 K. (*c*) Average temperature evolution over time with the reference temperature of 292 K. (*d*) Comparisons of the distance to the wall from the bubble centroid and the location of maximum temperature. (*e*) Temporal evolution of the distance from the maximum temperature location to the z axis. The collapse time is denoted by t_c and equals $t_c = 565.3$ μs.

the asymmetric flow environment caused by the proximity of the rigid wall that promotes far-wall flow motion for the heated gas and jet formation toward the wall. As a result, the temperature distribution becomes skewed, compressing vertically and stretching laterally into a pillow-like structure centred near the wall. This interplay between thermal and morphologic evolution is further quantified in figures 23(*d*)–25(*d*), which tracks the distances of both the centroid and the hottest spot from the wall for $\gamma = 0.97$, 1.64 and 2.14.

https://doi.org/10.1017/jfm.2026.11781 Published online by Cambridge University Press

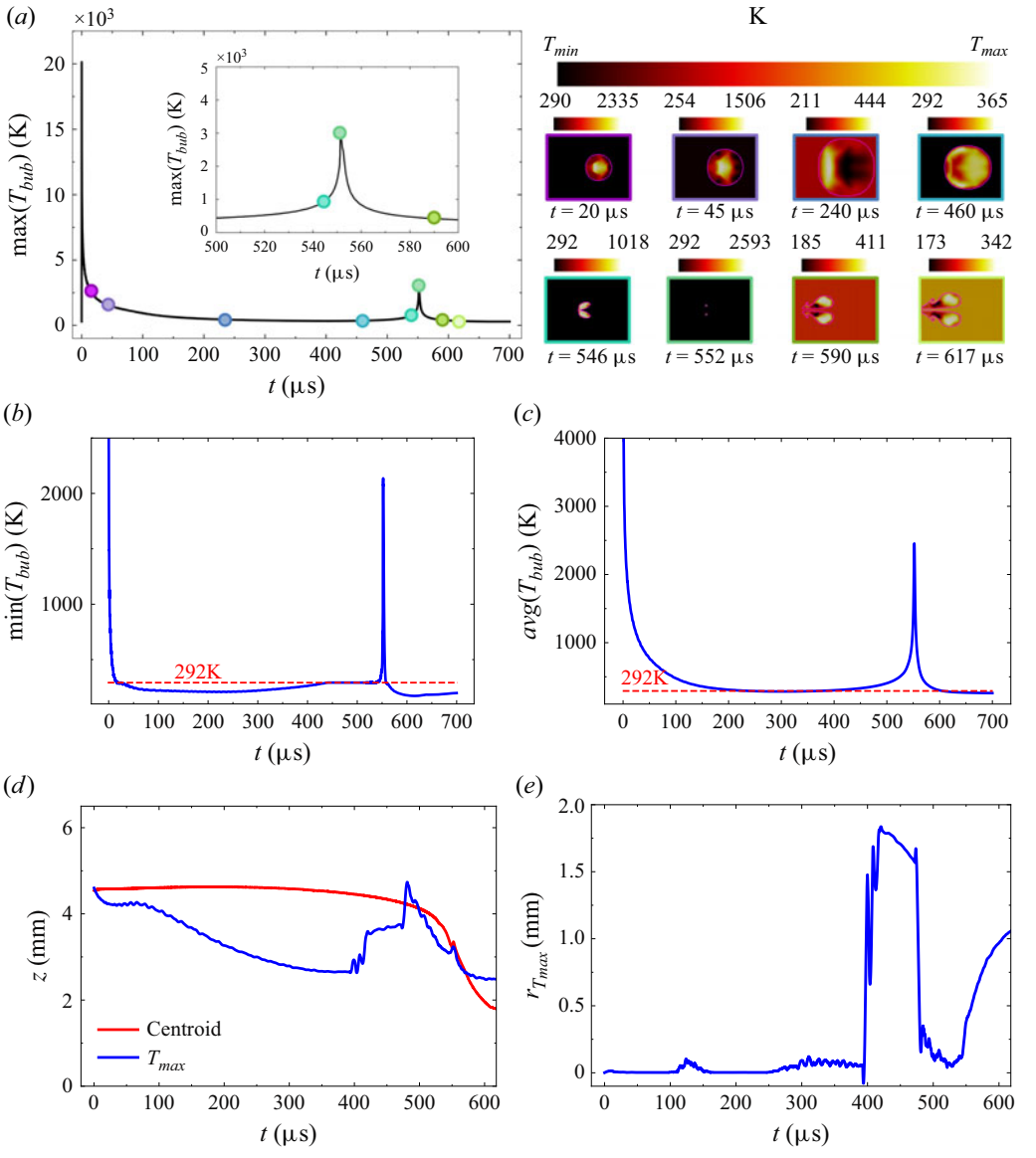


Figure 25. Temperature profile for $\gamma = 1.64$. (*a*) Maximum temperature evolution over time with the snapshots of the temperature fields at different times. The wall is aligned with the left boundary in each subfigure. The inset image represents the zoom-in of the maximum temperature evolution near bubble collapse. Minimum (*b*) and average (*c*) temperature evolution over time with the reference temperature of 292 K. (*d*) Comparisons of the distance to the wall from the bubble centroid and the location of maximum temperature. (*e*) Temporal evolution of the distance from the maximum temperature location to the z axis. The collapse time is denoted by t_c and equals $t_c = 552.1$ μs.

Figures 23(*b*)–25(*b*) show that during the expansion phase for all γ, certain regions within the bubble exhibit a temperature below the initial temperature of the surrounding liquid water (292 K). This undercooling phenomenon is primarily attributed to the quasi-adiabatic expansion that arises due to the extremely short time scales of the bubble growth of the order of 100 μs and characteristic advection transport time inside the bubble $t_{adv} \sim \max_t(R_{eq})/V \approx 100$ μs with gas velocity $V \lesssim 30\ \mathrm{m\ s^{-1}}$, compared with the thermal

https://doi.org/10.1017/jfm.2026.11781 Published online by Cambridge University Press

diffusion time $t_\delta = \max_t(R_{eq})^2/\delta$, where δ denotes thermal diffusivity for liquid water ($\approx 10^{-7}\text{m}^2\,\text{s}^{-1}$) and for water vapour ($\approx 2 \times 10^{-5}\ \text{m}^2\,\text{s}^{-1}$). For a maximum bubble radius $\max_t(R_{eq})$ of around 3 mm, $t_\delta \approx 100$ s in the liquid water and 0.5 s inside the bubble. This significant time scale difference between bubble growth and advection transport time, and thermal diffusion in both liquid water and water vapour indicates that the water vapour inside the bubble is effectively thermally isolated for $R_{eq} \gtrsim 3$ mm with a gas velocity $\lesssim 30\ \text{m}\,\text{s}^{-1}$. The volume of the bubble increases as the bubble expands, resulting in a drop in temperature due to the conservation of energy in the absence of significant heat exchange. Despite the presence of localised undercooled regions, the average temperature inside the bubble remains above the reference temperature of the surrounding liquid due to the persistence of high-temperature zones (see figures 23*c*–25*c*).

Notably, the hottest region remains much closer to the wall than the bubble centroid throughout the entire bubble lifetime for the three regimes. In the early phase following bubble generation, the rapid expansion leads to a strong transient for the velocity field. This results in the advection of high-temperature fluid towards the wall, while the bubble centroid moves slightly away from the wall, particularly for smallest γ, due to the fact that the bubble grows less on the near-wall interface than on the far-wall interface because of the presence of the wall causing asymmetric expansion that displaces the centroid away from the wall.

As the bubble continues to grow, the temperature location reaches a plateau in all cases (see, for example, the earliest 150 µs for $\gamma = 0.97$ in figure 23*d*), indicating that the early advection driven by strong velocity gradients has subsided. A second and slower convective time scale then becomes apparent, associated with the transport of heat through bulk flow rather than sharp gradients. This results in a slower, nearly linear decline of the maximum temperature position toward the wall, even as the bubble centroid continues to migrate away. As γ increases to 1.64, the influence of the wall becomes less dominant. The bubble exhibits a more symmetric expansion and there is a negligible shift of the bubble centroid away from the wall (as shown in figure 25*d*). The maximum temperature location remains closer to the wall than the bubble centroid, but its decline is more gradual, reflecting the weaker wall influence. In the case of $\gamma = 2.14$, the wall effect becomes minimal, leading to the most symmetric bubble growth dynamics among the three cases. While the hottest region still stays closer to the wall than the bubble centroid, its position is the most stable and least offset, reflecting the minimal influence of the wall at larger stand-off ratios.

Figures 23(*e*)–25(*e*) further illustrate the temporal evolution of the radial position of the maximum temperature point with respect to the z axis. During the initial expansion phase, the hottest region remains aligned with the z axis due to the nearly spherical bubble shape. However, as the bubble begins to shrink and approaches the wall, axial cooling dissipates heat more effectively along the z axis, displacing the maximum temperature location away from the z axis. During collapse, the bubble becomes highly compressed, and the maximum temperature region shifts back to the z axis, exhibiting a more uniform distribution. More details of bubble dynamics at t_c are reported in Appendix B. In the subsequent rebound phase, the bubble re-expands preferentially along the wall, further influencing the redistribution of heat inside the bubble.

4.4. *Thermodynamics inside the bubble*

The interplay between thermodynamic quantities is crucial for understanding the physical mechanism behind the cavitation bubble growth and collapse, especially as the

https://doi.org/10.1017/jfm.2026.11781 Published online by Cambridge University Press

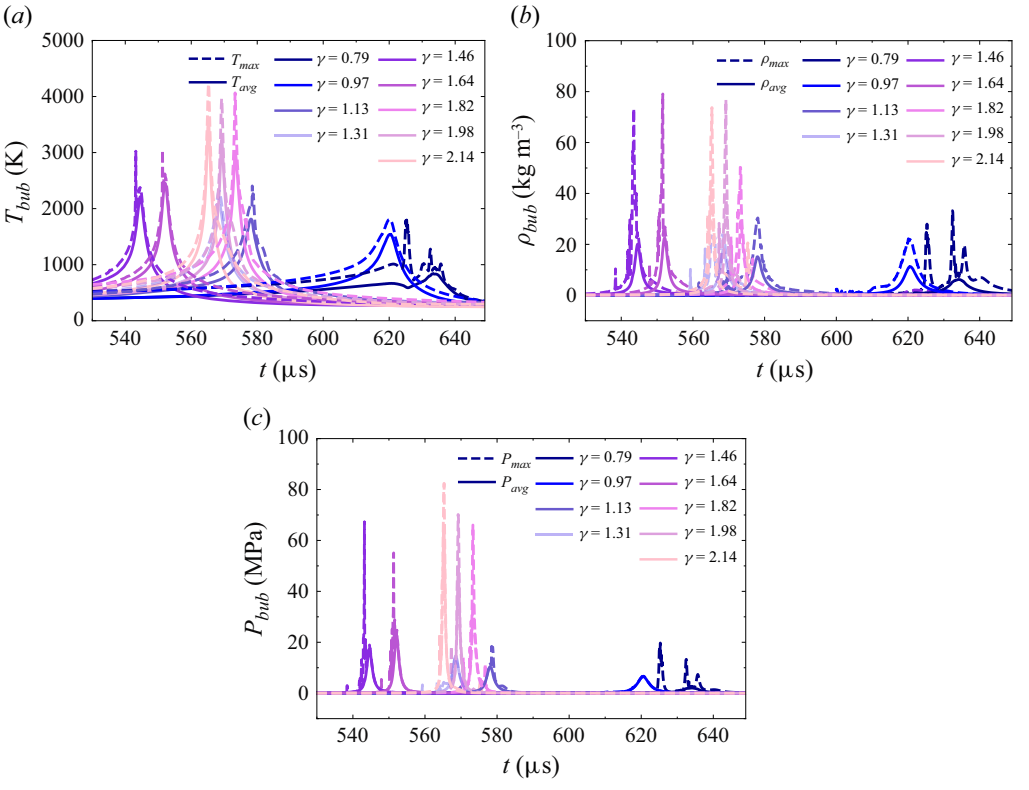


Figure 26. Temporal evolution of maximum and average temperature (*a*), density (*b*) and pressure (*c*) at different γ inside the bubble.

temperature can reach several thousands of Kelvin as the gas (Dular & Coutier-Delgosha 2013; Bidi 2023). To gain deeper insight into this mechanism, in this section we investigate the dynamics of density, pressure and temperature inside the bubble as a function of γ, which varies from 0.79 to 2.14. First of all, we present the temporal evolution of the maximum and mean value of each quantity at different γ. Then we analyse the relationship between the average internal thermodynamic quantities and γ. All the simulations are carried out using the absorption coefficient reported in table 2.

Figure 26 shows the temporal evolution of the maximum and average thermodynamic quantities as a function of γ. The results indicate that the thermodynamic properties inside the bubble are significantly influenced by γ, with all three quantities following a similar temporal trend. Specifically, they exhibit an increasing trend during the bubble collapse, reaching a spike at $t \approx t_c$ followed by a subsequent decrease during the bubble rebound phase. This behaviour can be explained by the EoS. As γ increases, the average gas pressure, temperature and density also increase during the first collapse phase, as shown in figure 27. This is expected, considering that spherical collapses ($\gamma \to \infty$) are the most energetic with the stronger pressure wave releases. In particular, figure 26(*a*) shows the evolution of maximum and average internal temperatures over time for different γ. During the bubble collapse phase, the internal temperature ranges from approximately 600 K to 3700 K. Additionally, as γ increases, the peak temperature occurs earlier as t_c is shorter. Specifically, as γ increases from 0.79 to 2.14, the time at which the peak temperature is reached ($t_{max(T_{avg})}$) decreases from 633.20 μs to 565.10 μs as t_c is shorter.

https://doi.org/10.1017/jfm.2026.11781 Published online by Cambridge University Press

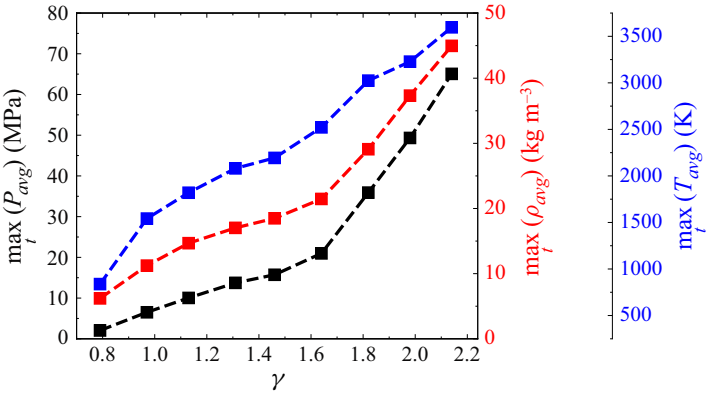


Figure 27. Relationship among the average internal pressure, temperature and density with γ during the first collapse phase.

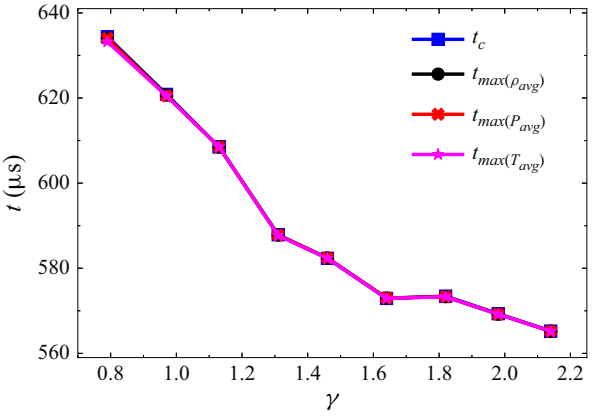


Figure 28. Comparison of collapse time t_c and the timing of maximum average internal pressure $t_{max(P_{avg})}$, density $t_{max(\rho_{avg})}$ and temperature $t_{max(T_{avg})}$ as functions of γ.

The differences among the collapse time t_c, the times corresponding to maximum average internal pressure $t_{max(P_{avg})}$, density $t_{max(\rho_{avg})}$ and temperature $t_{max(T_{avg})}$ are compared in figure 28. The results indicate that as γ increases, all characteristic times systematically decrease. This suggests that the bubble closer to the wall experiences a delayed collapse, while that farther away collapses more rapidly. Furthermore, the nearly perfect agreement among these four critical times implies that the peak in the average internal pressure, density and temperature occur almost simultaneously with the collapse, highlighting the strong coupling of thermodynamic and hydrodynamic processes during bubble collapse. Given the minimal difference among these time instants, we simplify our analysis by using t_c as the representative time for $t_{max(P_{avg})}$, $t_{max(\rho_{avg})}$ and $t_{max(T_{avg})}$ in the following discussion.

In terms of the density and pressure, figures 26(*b*) and 26(*c*) show the maximum and average internal bubble pressure and density evolution over time for γ from 0.79 to 2.14. Owing to compressibility, the bubble pressure and density increase during the collapse stage. The pressure and density change become extremely large when the bubble reaches its minimum radius at t_c. The peak bubble pressure and density are observed when γ is largest, i.e. $\gamma = 2.14$, at the first bubble collapse stage, with a value of approximately

https://doi.org/10.1017/jfm.2026.11781 Published online by Cambridge University Press

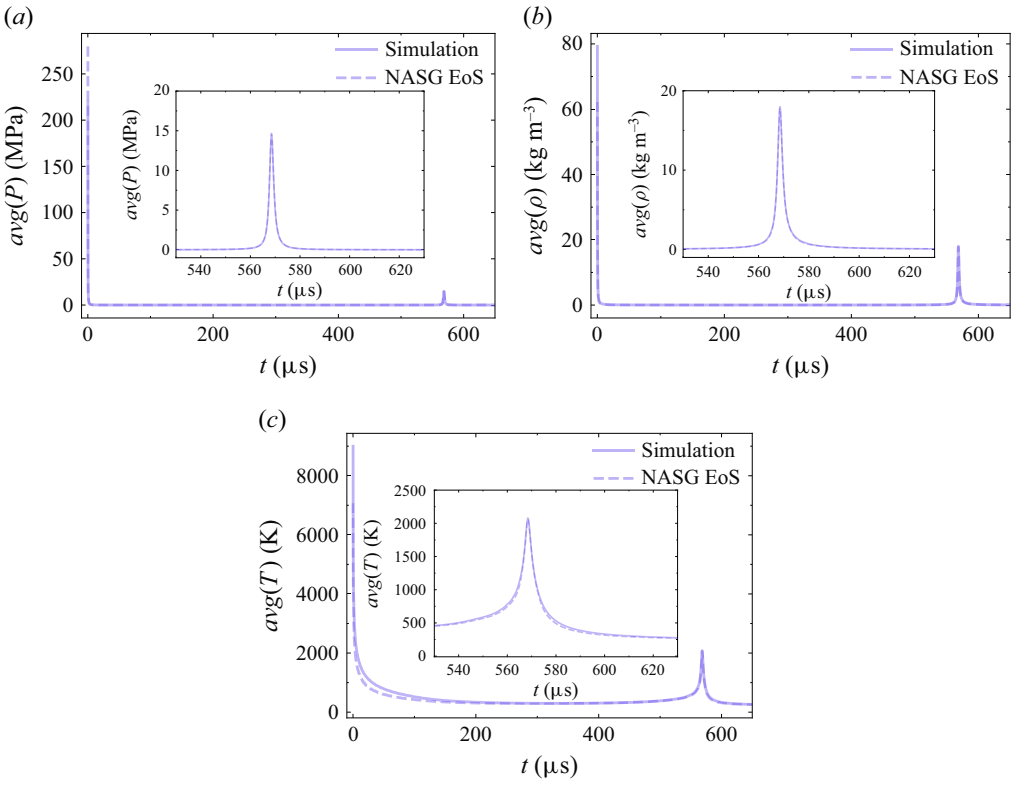


Figure 29. Comparison of the numerical solution for $\gamma = 1.31$ and NASG theoretical solution. (*a*) Temporal evolution of the average internal pressure. (*b*) Temporal evolution of the average internal density. (*c*) Temporal evolution of the average internal temperature. For each subfigure, the inset shows a zoomed-in section between 530–630 μs.

62 MPa and 45 kg m^{-3}. Subsequently, the bubble pressure and density decreased during the rebound stage.

Figure 29 shows a comparative analysis of one numerical case for $\gamma = 1.31$ and the theoretical predictions based on the NASG EoS assuming equilibrium for the average thermodynamic fields inside the bubble. Here, the NASG EoS is used to reconstruct one thermodynamic quantity from the other two. At each time instant, two spatially averaged quantities, for instance, bubble temperature and density, are inserted into the NASG EoS to compute the third quantity, i.e. pressure.

A noticeable difference is observed in terms of the temporal evolution of temperature (figure 29*c*) compared with pressure (figure 29*a*) and density (figure 29*b*). Temperature initially exhibits a non-negligible deviation, likely due to the fact that the liquid is preheated before bubble formation in laser-induced cavitation, creating a thermal memory effect that drives the initial evolution of the bubble significantly out-of-average equilibrium. After reaching its peak, temperature decreases more gradually, following a smooth transition rather than the rapid drops observed in pressure and density. This behaviour can be attributed to energy dissipation and heat retention, as well as the effects of thermal conductivity and heat diffusion. The internal energy, which governs temperature, dissipates progressively rather than sharply. Heat diffusion occurs at a slower rate quantified by $t_\delta = \min_t (R_{eq})^2/\delta$, where δ denotes thermal diffusivity, at around

https://doi.org/10.1017/jfm.2026.11781 Published online by Cambridge University Press

$10^{-7}\,\mathrm{m^2\,s^{-1}}$ in the liquid water and $2\times10^{-5}\,\mathrm{m^2\,s^{-1}}$ in the gas. For a minimum bubble radius $\min_t(R_{eq})$ of around 0.5 mm, t_δ reaches approximately 2.5 s in the liquid water and 1 s in the gas. Conversely, the rapid compression and rebound process is governed by the Rayleigh collapse time, which governs $\ddot{R}$, i.e. $t_R \approx 0.915 \min_t(R_{eq})\sqrt{\rho/\Delta p} \approx 46\,\mu\mathrm{s}$, controlling the dynamics of pressure and density. $t_\delta \gg t_R$ leads to a more continuous and prolonged cooling phase.

Despite this deviation, the overall agreement across all thermodynamic variables demonstrates that spatial averaging provides a robust framework for linking non-equilibrium numerical simulations with average thermodynamic equilibrium predictions of the NASG EoS. This consistency validates that the averaged thermodynamic fields can reliably be modelled as in average thermodynamic equilibrium for most of the bubble lifetime, capturing the essential physics of bubble dynamics and cavitation phenomena near a wall.

5. Conclusion

In this work, a recent laser–fluid computational model was applied to study the physics behind a water vapour bubble induced by laser near a solid wall. The computational model combines laser energy absorption, vaporisation and thermodynamics of a compressible two-phase fluid flow, enabling the simulation of bubble formation, growth and collapse without predefining an initial bubble. The solver was employed for the first time for studying a wall-detached bubble. A broad range of stand-off ratios $\gamma \in [0.79, 2.14]$ was investigated to assess the influence on the interfacial dynamics, collapse regimes and thermodynamics inside the bubble. Despite neglecting condensation, surface tension and viscous effects, the model reliably reproduces both qualitatively and quantitatively the experimental measurements for interfacial and wall pressure dynamics of a millimetric laser-induced bubble, provided that the right absorption coefficient is set to account for initial laser thermal energy absorption. To the best of the authors' knowledge, this is the first time that such a detailed comparison is done on so many dynamical experimental measurements.

The comparison of interfacial dynamics between numerical simulations and experimental measurements demonstrates that the present model reliably reproduces the interfacial dynamics of laser-induced cavitation bubbles across a wide range of stand-off ratios. The simulated bubble shapes, collapse times and geometric evolution exhibit excellent agreement with experimental measurements, particularly during the expansion and early collapse stages. Minor discrepancies near the final collapse are attributed to sensitivity to the absorbed energy and experimental measurement uncertainties at small scales. The model accurately predicts the migration of the bubble centroid and the asymmetric interface motion leading to jet formation. Furthermore, the near-wall and far-wall interface velocities are captured with high fidelity, especially when the absorption coefficient is properly calibrated, confirming the model's ability to resolve the strongly inertial jetting and rebound phenomena. These results validate the capability of the proposed two-phase compressible model to predict the complex interfacial dynamics of millimetric laser-induced bubbles near a wall.

Three distinct collapse regimes have been identified in the simulations, consistent with the experimental identification by Subramanian *et al.* (2026). The torus collapse regime occurs for $\gamma \leqslant 0.97$, the mixed tip-and-torus collapse regime for $1.13 \leqslant \gamma \leqslant 1.46$ and the tip collapse regime for $\gamma \geqslant 1.64$. The wall pressure dynamics is found to be significantly affected by the initial energy absorbed by the gas phase solely in the mixed tip-and-torous collapse regime. This has been confirmed by additional simulations (not shown) for

https://doi.org/10.1017/jfm.2026.11781 Published online by Cambridge University Press

which we considered the pure-torous collapse and pure-tip collapse regimes for a range of absorption coefficients of 90 000 m^{-1} to 110 000 m^{-1} without finding any major deviations to the reported results.

After validating the robustness of the computational model against experimental results, the simulations reveal that increasing γ leads to a more symmetric expansion, delayed jet impact and higher collapse pressures and temperatures. Conversely, smaller γ enhances the wall influence, resulting in asymmetric bubble expansion and early jet formation. Despite these quantitative differences, all cases share a rapid expansion, quasi-uniform bubble pressure at maximum volume, jet formation and violent collapse accompanied by strong pressure and temperature peaks. The simulations thus establish a coherent physical picture of how bubble–wall interaction controls the evolution of pressure, temperature and interface morphology across different collapse regimes.

The analysis of the thermodynamic evolution inside the bubble reveals a strong dependence on the stand-off ratio γ. Both maximum and average values of pressure, density and temperature exhibit similar temporal behaviour, characterised by a sharp rise before collapse, a pronounced peak at $t \approx t_c$ and a rapid decay during rebound. Increasing γ leads to higher peak magnitudes and an earlier occurrence of these peaks, indicating that more spherical collapses produce stronger compression and heating effects. Comparison with the NASG EoS shows that spatially averaged pressure and density fields from the simulations follow equilibrium trends, even though the bubble dynamics is strongly non-equilibrium. The slower thermal relaxation relative to mechanical equilibrium highlights the persistence of out-of-average-equilibrium effects on the temperature, hence showing the importance of bubble temperature gradients after generation and after collapse. The bubble is far from an average thermodynamic equilibrium in its initial dynamics, especially for the temperature, which suggests that modelling approaches starting from a small bubble size and adjusted average pressure and density could lead to significant discrepancies in the evolution of a simulated bubble if the average temperature is set by enforcing the EoS. This is routinely done in the scientific literature and our study demonstrates that millimetric laser-induced bubbles are far from being realistically represented by such initial conditions. This has also been directly demonstrated comparing different initial conditions in our previous paper (Wang *et al.* 2026).

As a natural consequence of this conclusion, we point out that the most robust condition to model seems to be the bubble at its maximum volume, for which average thermodynamical quantities verify the equations of state. We however stress the need for modelling temperature and pressure gradients, as also pointed out in our previous study by Yang *et al.* (2025).

Supplementary movies. Supplementary movies are available at https://doi.org/10.1017/jfm.2026.11781.

Funding. This work has been financially supported by the Chinese Scholarship Council (CSC) for B. Wang (student number 202206240030) and Z. Yang (student number 202008310185).

Declaration of interests. The authors report no conflict of interest.

Appendix A. Effect of EoS parameter values

We find that the behaviour of the bubble in the current laser–fluid computational framework can be affected by the choice of EoS. Here, we perform an additional simulation using a different set of EoS parameter values adopted from Métayer *et al.* (2016), while keeping all other physical and numerical parameters unchanged. Figure 30 compares the evolution of the equivalent bubble radius and wall pressure peak obtained from two different references of EoS parameter values for $\gamma = 1.82$. Overall, both simulations

https://doi.org/10.1017/jfm.2026.11781 Published online by Cambridge University Press

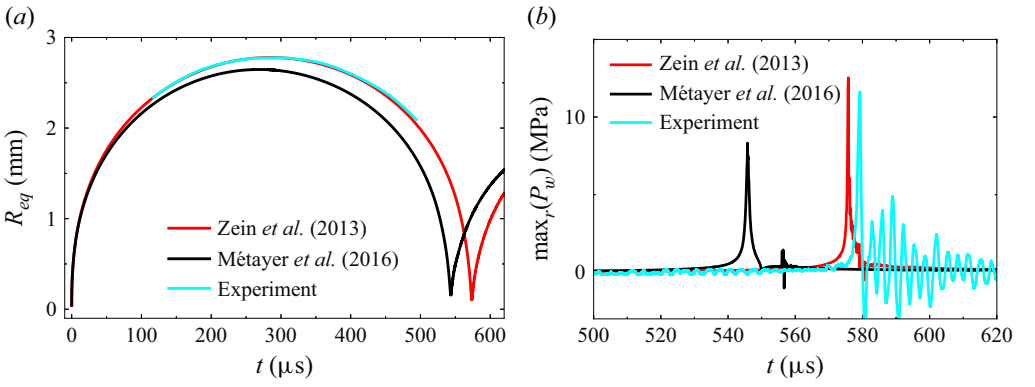


Figure 30. Comparison of simulation results obtained with different EoS parameter values for $\gamma = 1.82$. (*a*) Evolution of the equivalent radius of the bubble. (*b*) Wall pressure peak.

reproduce similar bubble dynamics over the entire cycle, with the bubble reaching its minimum size and wall pressure peak at the collapse time.

Nevertheless, some quantitative differences can be observed between the two cases.The maximum equivalent bubble radius obtained with the parameters of Zein *et al.* (2013) is about 2.78 mm with collapse occurring at approximately 573 μs. In contrast, when using the parameters of Métayer *et al.* (2016), the maximum radius is slightly smaller, at 2.65 mm and the collapse occurs earlier at around 543 μs. Regarding the wall pressure, the simulation with Zein *et al.* (2013) parameters yields pressure peaks of 12.5 MPa at collapse, and matches well with the experimental measurements by Subramanian *et al.* (2026), whereas the corresponding value with Métayer *et al.* (2016) parameters is 8.3MPa.

Appendix B. Temperature, density, pressure and velocity field inside the bubble at t_c for three cases

The axisymmetric simulation results for three different γ, i.e. $\gamma = 0.97$. 1.64 and 2.14, presented in figure 31 together with figure 32, which shows the temperature, density, pressure and velocity distribution outside and inside the bubble, along with the liquid–gas interface depicted in a magenta colour at t_c. Insets highlight the internal field of the bubble. Inside the bubble, the maximum temperature increases with γ, reaching approximately 1793 K, 2833 K and 4226 K for $\gamma = 0.97$, 1.64 and 2.14, respectively. Similarly, the peak density rises from approximately 21 kg m^{-3} for $\gamma = 0.97$ to 67 kg m^{-3} for $\gamma = 2.14$, highlighting stronger gas compression at larger distances from the wall. The internal pressure exhibits a significant increase, with maximum values of approximately 6.6 MPa, 23 MPa and 79 MPa, respectively. The velocity inside the bubble (see figure 32) also intensifies as γ increases, with its magnitude rising from approximately 97 m s^{-1} for $\gamma = 0.97$ to 240 m s^{-1} for $\gamma = 2.14$. These trends suggest that at larger bubble centroid–wall distances, the internal thermodynamic extremes become more pronounced, leading to stronger compressive and convective effects within the bubble. Besides, the bubble collapse becomes more spherical as γ increases. The velocity field depicted in figure 32 reveals that both flow intensities inside and outside the bubble increases with γ. The contraction speed of the bubble interface differs in the axial and radial directions, particularly for small γ, where the radial collapse is faster, causing the interface of the bubble to extend farther from the z axis, while the axial velocity becomes dominant as γ increases. This more axis-focused collapse trend is further supported by figure 33,

https://doi.org/10.1017/jfm.2026.11781 Published online by Cambridge University Press

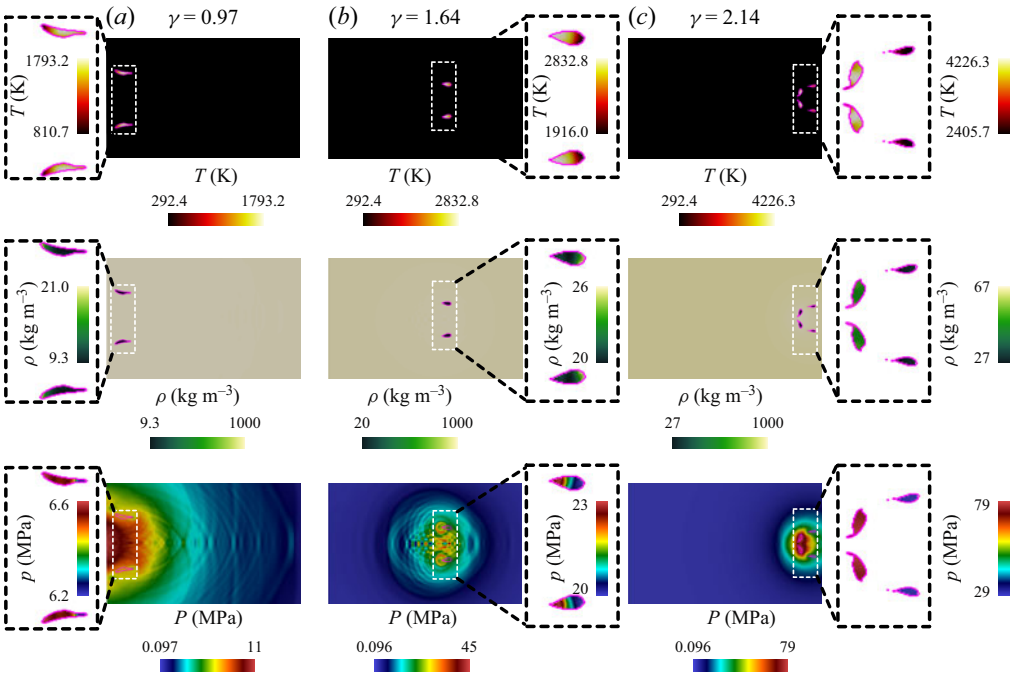


Figure 31. Temperature, density and pressure field (from top to bottom) at the collapse time for stand-off ratios (*a*) $\gamma = 0.97$, (*b*) $\gamma = 1.64$, (*c*) $\gamma = 2.14$. The collapse time is denoted as t_c and corresponds to $t_c = 620.5\,\mu$s for $\gamma = 0.97$, $t_c = 573\,\mu$s for $\gamma = 1.64$, $t_c = 565.2\,\mu$s for $\gamma = 2.14$. The wall is aligned with the left boundary in each subfigure. The inset images on the side magnify the bubble interior fields.

which shows that both minimum and maximum quantities move closer to the z axis as γ increases, indicating that high intensity regions concentrate near the centreline.

Appendix C. Influence of the numerical boundary on the bubble shape

The potential reflection of shock waves at the numerical boundaries was carefully considered in the present simulations. To minimise boundary effects, the computational domain was chosen to be sufficiently large (55 times the maximum bubble size), and Neumann conditions were applied at the far-field boundary to ensure that outgoing waves do not reflect back. Moreover, upon an increase of the numerical domain, we do not observe any significant change in the bubble size during the early stage (tests done for $\gamma = 1.82$; see figure 34). Regarding the effect of the solid wall, the bubble shape during the generation develops primarily along the laser beam direction. At this early time, e.g. at 78 ns, the bubble is sufficiently far from the wall compared with its current size, and the influence of the wall on the bubble shape during the generation process is negligible. The early bubble shape shows that the side closer to the laser plane is slightly wider than the opposite side at the nucleation point (see figure 35), which is consistent with experimental observations reported by Gonzalez-Avila *et al.* (2021).

Appendix D. Determination of equivalent bubble radius from the experimental visualisation

In the experiment, the equivalent radius of the bubble is measured from the top view using high-speed imaging, as shown in figure 36. There are generally five steps in our bubble characterisation protocol. (i) All relevant frames are extracted from the high-speed

https://doi.org/10.1017/jfm.2026.11781 Published online by Cambridge University Press

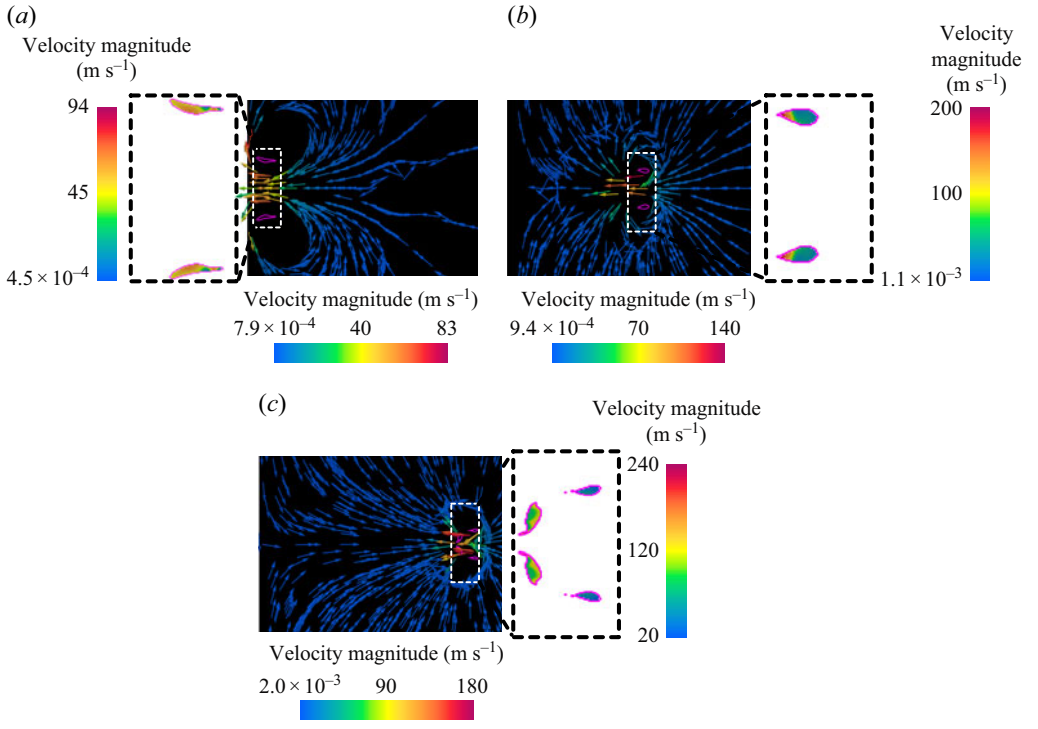


Figure 32. Velocity field at the collapse time for stand-off ratios (*a*) $\gamma = 0.97$, (*b*) $\gamma = 1.64$, (*c*) $\gamma = 2.14$. The collapse time is denoted as t_c and corresponds to $t_c = 620.5\,\mu$s for $\gamma = 0.97$, $t_c = 573\,\mu$s for $\gamma = 1.64$, $t_c = 565.2\,\mu$s for $\gamma = 2.14$. The wall is aligned with the left boundary in each subfigure. The inset images on the side magnify the bubble interior fields.

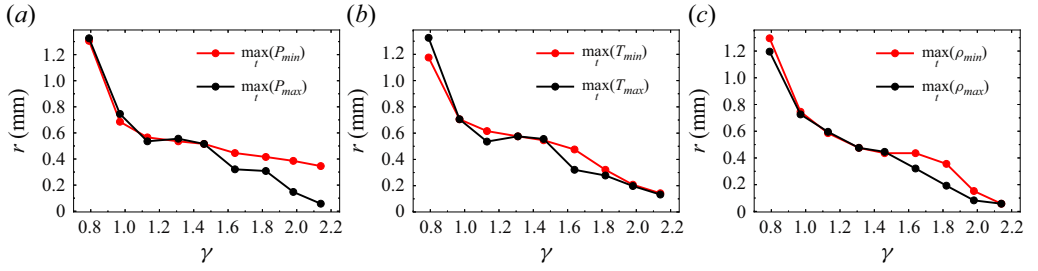


Figure 33. Radial position inside the bubble of peak values of the maximum and minimum pressure, temperature and density evolved over time as a function of γ.

recordings. (ii) For each frame, the bubble interface coordinates (r_b, z_b) are identified based on the index refraction contrast between liquid water and water vapour. (iii) The problem is simplified by assuming that the bubble growth is axisymmetric, allowing us to reflect part of the interfacial coordinates (r_b, z_b) with respect to the axis. (iv) An in-house MATLAB code is then developed to fit the bubble interface using the fitting function $r_i^2 = a_0^2 - (z_i - a_1)^2 \times (1 + (a_2/z_i^{a_3}))$, where a_0,a_1,a_2,a_3 are fitting parameters and z_i and r_i denote axial and radial coordinates of the fitted interface. (v) The bubble volume is computed by revolving the fitted interface about the symmetry axis, and the equivalent bubble radius is finally obtained from the calculated volume assuming a spherical bubble of equal volume. For more details on the fitting function, we refer the reader to Yang *et al.* (2025).

https://doi.org/10.1017/jfm.2026.11781 Published online by Cambridge University Press

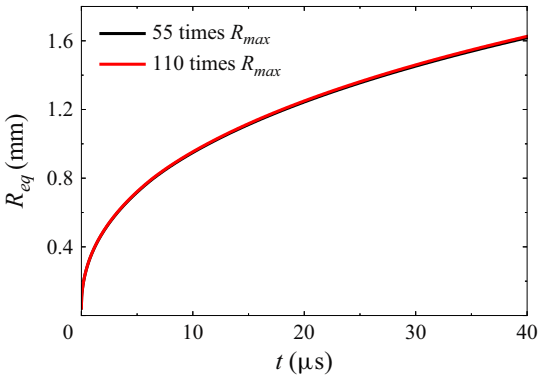


Figure 34. Comparison of the bubble radius at the numerical domain size of 55 and 110 times the maximum bubble size.

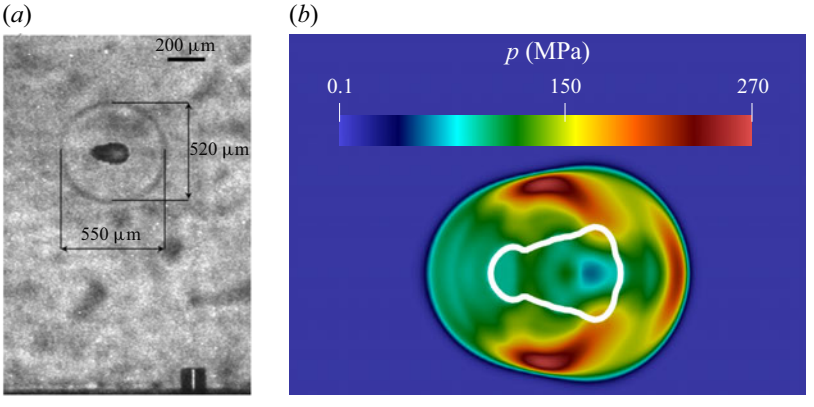


Figure 35. (*a*) Experimental bubble shape and (*b*) computational bubble shape at 78 ns after the laser is on.

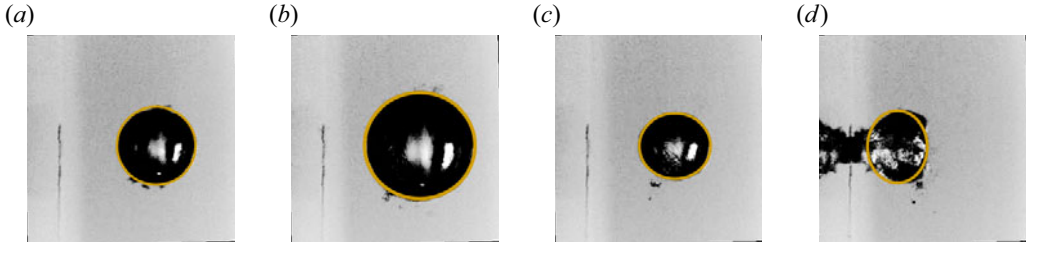


Figure 36. Case $\gamma = 1.64$. The experimental top view of a cavitation bubble is indicated in black, while the orange mark presents the bubble shape calculated by our fitting algorithm. From left to right, the snapshots correspond to $t = 65$ μs, 273 μs, 520 μs, 741 μs, respectively, while the collapse time is $t_c = 572$ μs.

This method provides accurate results during the expansion and early shrink phase (see figure 36*a–c*), where the bubble shape remains relatively spherical and approximately axisymmetric. During the late collapse and rebound phases, however, the bubble interface becomes highly deformed and non-elliptic in the camera view due to the microjet penetration (see the experimental image reported in figure 36*d*). Under these conditions, the fitting function can no longer guarantee reliable volume reconstruction, and the experiment equivalent radius after the late collapse and rebound phases are therefore not included in the numerical validation. In particular, as for a comparison after the first

https://doi.org/10.1017/jfm.2026.11781 Published online by Cambridge University Press

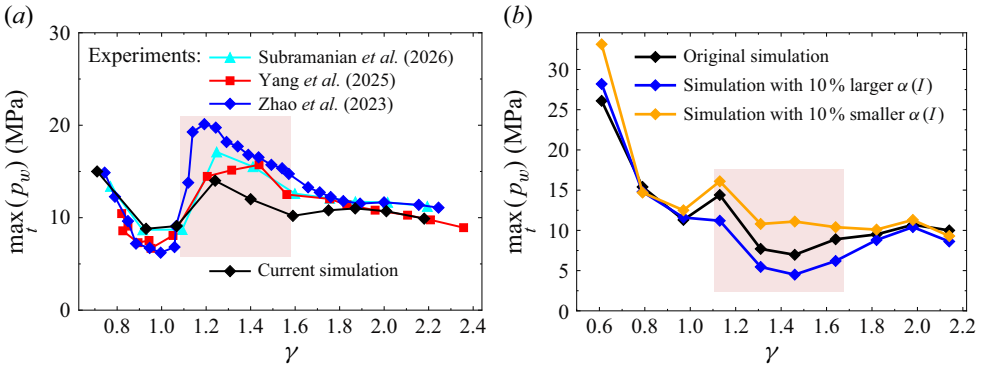


Figure 37. (*a*) Comparison of the maximum wall pressure $\max_t(p_w)$ among three experimental measurements by Zhao & Coutier-Delgosha (2023), Yang *et al.* (2025), Subramanian *et al.* (2026), respectively, and the current numerical result. (*b*) Sensitivity of the maximum pressure at the wall centre to the absorption coefficient for all stand-off ratios γ in the present study. The absorption coefficient is denoted by $\alpha(I)$.

rebound, phase change is known to be significant starting from the first rebound phase (Yin *et al.* 2021). Our physical model does not include phase transition beyond bubble generation, hence, the comparison between our simulations and the experiments is of limited use beyond the first collapse.

Appendix E. Sensitivity of the mixed tip-and-torus collapse regime to the initial condition

Figure 37(*a*) shows three independent experimental measurements conducted by Zhao & Coutier-Delgosha (2023), Yang *et al.* (2025), Subramanian *et al.* (2026) within the same laboratory using the same apparatus. A significant statistical variance is observed in the mixed tip-and-torus collapse regime ($1.13 \leqslant \gamma \leqslant 1.46$). In contrast, such variability is not observed in the purely torus ($\gamma < 1.13$) and purely tip ($\gamma > 1.46$) collapse regimes. This discrepancy indicates that the mixed torus-and-tip regime is highly sensitive to initial conditions, making the repeatability of multiple experiments difficult to achieve even under controlled conditions. Consequently, attempting a strict quantitative prediction by simulation in this regime is inherently limited.

To further support this interpretation, we investigate the sensitivity of different collapse regimes to a change of the absorption coefficient, as shown in figure 37(*b*). The absorption coefficient $\alpha(I)$ increases and decreases slightly by 10 %, respectively, for each γ, and the resulting changes in the maximum pressure at the wall centre are analysed. The results clearly show that the mixed regime shows a much stronger sensitivity to variation in the absorption coefficient $\alpha(I)$ compared with purely tip and purely torus collapse regimes. This confirms that the strong sensitivity is specific to the mixed regime and not observed in the two other collapse regimes.

References

ARNDT, R.E.A. 1981 Cavitation in fluid machinery and hydraulic structures. *Annu. Rev. Fluid Mech.* **13** (1), 273–326.

ASHOKKUMAR, M. 2011 The characterization of acoustic cavitation bubbles – an overview. *Ultrason. Sonochemistry* **18** (4), 864–872.

ASHOKKUMAR, M., LEE, J., KENTISH, S. & GRIESER, F. 2007 Bubbles in an acoustic field: an overview. *Ultrason. Sonochemistry* **14** (4), 470–475.

AVILA, S.R.G., SONG, C. & OHL, C.-D. 2015 Fast transient microjets induced by hemispherical cavitation bubbles. *J. Fluid Mech.* **767**, 31–51.

https://doi.org/10.1017/jfm.2026.11781 Published online by Cambridge University Press

BALZ, R., NAGY, I.G., WEISSER, G. & SEDARSKY, D. 2021 Experimental and numerical investigation of cavitation in marine Diesel injectors. *Intl J. Heat Mass Transfer* **169**, 120933.

BIDI, S. 2023 Numerical study of thermal effects during bubble collapse. Theses, Sorbonne Université, France.

BRENNEN, C.E. 2014 *Cavitation and Bubble Dynamics*. Cambridge University Press.

BRUJAN, E.-A., NAHEN, K., SCHMIDT, P. & VOGEL, A. 2001 Dynamics of laser-induced cavitation bubbles near an elastic boundary. *J. Fluid Mech.* **433**, 251–281.

BUSSMANN, A., RIAHI, F., GÖKCE, B., ADAMI, S., BARCIKOWSKI, S. & ADAMS, N.A. 2023 Investigation of cavitation bubble dynamics near a solid wall by high-resolution numerical simulation. *Phys. Fluids* **35** (1), 016115.

CRISTOFARO, M., EDELBAUER, W., KOUKOUVINIS, P. & GAVAISES, M. 2020 A numerical study on the effect of cavitation erosion in a diesel injector. *Appl. Math. Model.* **78**, 200–216.

CUI, P., ZHANG, A.-M., WANG, S. & KHOO, B.C. 2018 Ice breaking by a collapsing bubble. *J. Fluid Mech.* **841**, 287–309.

DULAR, M. & COUTIER-DELGOSHA, O. 2013 Thermodynamic effects during growth and collapse of a single cavitation bubble. *J. Fluid Mech.* **736**, 44–66.

DULAR, M. *et al.*et al. 2019 High speed observation of damage created by a collapse of a single cavitation bubble. *Wear* **418**, 13–23.

FUSTER, D. & POPINET, S. 2018 An all-Mach method for the simulation of bubble dynamics problems in the presence of surface tension. *J. Comput. Phys.* **374**, 752–768.

GENSHENG, L., ZHONGHOU, S., CHANGSHAN, Z., DEBIN, Z. & HONGBING, C. 2005 Investigation and application of self-resonating cavitating water jet in petroleum engineering. *Petrol. Sci. Technol.* **23** (1), 1–15.

GONZALEZ-AVILA, S.R., DENNER, F. & OHL, C.-D. 2021 The acoustic pressure generated by the cavitation bubble expansion and collapse near a rigid wall. *Phys. Fluids* **33** (3), 032118.

HARRISON, M. 1952 An experimental study of single bubble cavitation noise. *J. Acoust. Soc. Am.* **24**, 454–454.

HERBERT, E., BALIBAR, S. & CAUPIN, F. 2006 Cavitation pressure in water. *Phys. Rev. E—Stat. Nonlinear Soft Matt. Phys.* **74** (4), 041603.

IIDA, Y., ASHOKKUMAR, M., TUZIUTI, T., KOZUKA, T., YASUI, K., TOWATA, A. & LEE, J. 2010 Bubble population phenomena in sonochemical reactor: I estimation of bubble size distribution and its number density with pulsed sonication – laser diffraction method. *Ultrason. Sonochemistry* **17** (2), 473–479.

KADIVAR, E., EL MOCTAR, O., SKODA, R. & LÖSCHNER, U. 2021 Experimental study of the control of cavitation-induced erosion created by collapse of single bubbles using a micro structured riblet. *Wear* **486**, 204087.

KARIMI, A. & MARTIN, J.L. 1986 Cavitation erosion of materials. *Intl Mater. Rev.* **31** (1), 1–26.

KHLIFA, I., COUTIER-DELGOSHA, O., FUZIER, S., VABRE, A. & FEZZAA, K. 2013 Velocity measurements in cavitating flows using fast X-ray imaging. In *Congrés Français de Mécanique*.

KRÖNINGER, D., KÖHLER, K., KURZ, T. & LAUTERBORN, W. 2010 Particle tracking velocimetry of the flow field around a collapsing cavitation bubble. *Exp. Fluids* **48** (3), 395–408.

LAGUNA-CAMACHO, J.R., LEWIS, R., VITE-TORRES, M. & MÉNDEZ-MÉNDEZ, J.V. 2013 A study of cavitation erosion on engineering materials. *Wear* **301** (1–2), 467–476.

LAUTERBORN, W. & KURZ, T. 2010 Physics of bubble oscillations. *Rep. Prog. Phys.* **73** (10), 106501.

LECHNER, C., LAUTERBORN, W., KOCH, M. & METTIN, R. 2020 Jet formation from bubbles near a solid boundary in a compressible liquid: numerical study of distance dependence. *Phys. Rev. Fluids* **5**, 093604.

LI, Y., FENG, G., LI, X., SI, Q. & ZHU, Z. 2018 An experimental study on the cavitation vibration characteristics of a centrifugal pump at normal flow rate. *J. Mech. Sci. Technol.* **32** (10), 4711–4720.

LINDAU, O. & LAUTERBORN, W. 2003 Cinematographic observation of the collapse and rebound of a laser-produced cavitation bubble near a wall. *J. Fluid Mech.* **479**, 327–348.

MAEDA, K., COLONIUS, T., KREIDER, W., MAXWELL, A. & BAILEY, M. 2016 Modeling and experimental analysis of acoustic cavitation bubble clouds for burst-wave lithotripsy. *J. Acoust. Soc. Am.* **140**, 3307–3307.

MARBLE, C.B., CLARY, J.E., NOOJIN, G.D., O'CONNOR, S.P., NODURFT, D.T., WHARMBY, A.W., ROCKWELL, B.A., SCULLY, M.O. & YAKOVLEV, V.V. 2018 Z-scan measurements of water from 1150 to 1400 nm. *Opt. Lett.* **43** (17), 4196–4199.

MIŠÍK, V. & RIESZ, P. 1996 EPR study of free radicals induced by ultrasound in organic liquids II. Probing the temperatures of cavitation regions. *Ultrason. Sonochemistry* **3** (1), 25–37.

MÉTAYER, O.L., SAUREL, R., MÉTAYER, O.L. & SAUREL, R. 2016 The Noble-Abel stiffened-gas equation of state 046102. *Phys. Fluids* **28** (4), 046102.

NGUYEN, Q.-T., KADIVAR, E., PHAN, T.-H., NGUYEN, V.-T., EL MOCTAR, O. & PARK, W.-G. 2025 Effects of free surface on dynamics of a laser-induced cavitation bubble near horizontal rigid wall. *Ocean Engng* **319**, 120258.

https://doi.org/10.1017/jfm.2026.11781 Published online by Cambridge University Press

PHAN, T.-H., KADIVAR, E., NGUYEN, V.-T., EL MOCTAR, O. & PARK W.-G. 2022*a* Thermodynamic effects on single cavitation bubble dynamics under various ambient temperature conditions. *Phys. Fluids* **34** (2), 023318.

PHAN, T.-H., NGUYEN, V.-T., DUY, T.-N., KIM, D.-H. & PARK, W.-G. 2022*b* Influence of phase-change on the collapse and rebound stages of a single spark-generated cavitation bubble. *Intl J. Heat Mass Transfer* **184**, 122270.

POPE, R.M. & FRY, E.S. 1997 Absorption spectrum 380–700 nm of pure water. II. Integrating cavity measurements. *Appl. Opt.* **36** (33), 710–8723.

PRESO, D.B., FUSTER, D., SIEBER, A.B., OBRESCHKOW, D. & FARHAT, M. 2024 Vapor compression and energy dissipation in a collapsing laser-induced bubble. *Phys. Fluids* **36** (3), 033342.

RAE, J., ASHOKKUMAR, M., EULAERTS, O., VON SONNTAG, C., REISSE, J., GRIESER, F. 2005 Estimation of ultrasound induced cavitation bubble temperatures in aqueous solutions. *Ultrason. Sonochemistry* **12** (5), 325–329.

REN, X.D., HE, H., TONG, Y.Q., REN, Y.P., YUAN, S.Q., LIU, R., ZUO, C.Y., WU, K., SUI, S. & WANG, D.S. 2016 Experimental investigation on dynamic characteristics and strengthening mechanism of laser-induced cavitation bubbles. *Ultrason. Sonochemistry* **32**, 218–223.

REUTER, F., LAUTERBORN, S., METTIN, R. & LAUTERBORN, W. 2017 Membrane cleaning with ultrasonically driven bubbles. *Ultrason. Sonochemistry* **37**, 542–560.

REZAEE, S., KADIVAR, E. & EL MOCTAR, O. 2025 Molecular dynamics-based approach for laser-induced cavitation bubbles: bridging experimental and hybrid analytical–computational approaches. *Langmuir* **41** (29), 19071–19087.

ROCKWELL, B.A., ROACH, W.P., ROGERS, M.E., MAYO, M.W., TOTH, C.A., CAIN, C.P. & NOOJIN, G.D. 1993 Nonlinear refraction in vitreous humor. *Opt. Lett.* **18** (21), 1792–1794.

SAADE, Y., LOHSE, D. & FUSTER, D. 2023 A multigrid solver for the coupled pressure-temperature equations in an all-Mach solver with VoF. *J. Comput. Phys.* **476**, 111865.

SOYAMA, H., CHIGHIZOLA, C.R. & HILL, M.R. 2021 Effect of compressive residual stress introduced by cavitation peening and shot peening on the improvement of fatigue strength of stainless steel. *J. Mater. Process. Technol.* **288**, 116877.

SUBRAMANIAN, R.K., YANG, Z., ROMANÒ, F. & COUTIER-DELGOSHA, O. 2026 Single bubble collapse near a wall: pressure wave and microjet impact. *Phys. Fluids* **38** (4), 046114.

SUPPONEN, O., OBRESCHKOW, D., KOBEL, P., TINGUELY, M., DORSAZ, N. & FARHAT, M. 2017 Shock waves from nonspherical cavitation bubbles. *Phys. Rev. Fluids* **2** (9), 093601.

TINGUELY, M. 2013 The effect of pressure gradient on the collapse of cavitation bubbles in normal and reduced gravity. *PhD thesis*, Verlag nicht ermittelbar. Doctoral dissertation, École Polytechnique Fédérale De Lausanne.

TOMITA, Y., ROBINSON, P.B., TONG, R.P. & BLAKE, J.R. 2002 Growth and collapse of cavitation bubbles near a curved rigid boundary. *J. Fluid Mech.* **466**, 259–283.

TSOCHATZIDIS, N.A., GUIRAUD, P., WILHELM, A.M. & DELMAS, H. 2001 Determination of velocity, size and concentration of ultrasonic cavitation bubbles by the phase-Doppler technique. *Chem. Engng Sci.* **56** (5), 1831–1840.

WALMSLEY, A.D., LAIRD, W.R.E. & WILLIAMS, A.R. 1988 Dental plaque removal by cavitational activity during ultrasonic scaling. *J. Clin. Periodontology* **15** (9), 539–543.

WANG, B., YANG, Z. & ROMANÒ, F. 2026 Cavitation bubble near a wall: sensitivity to modeling conditions. *Technische Mech.-Eur. J. Engng Mecha.* **46** (1), 66–77.

YANG, Z., WANG, B. & ROMANÒ, F. 2025 Bubble collapse near a wall: a numerical study on the impact of physical mechanisms for a bubble initially at rest. *Intl J. Multiphase Flow* **196**, 105567.

YIN, J., ZHANG, Y., ZHU, J., LV, L. & TIAN, L. 2021 An experimental and numerical study on the dynamical behaviors of the rebound cavitation bubble near the solid wall. *Intl J. Heat Mass Transfer* **177**, 121525.

ZEIN, A., HANTKE, M. & WARNECKE, G. 2013 On the modeling and simulation of a laser-induced cavitation bubble. *Intl J. Numer. Meth. Fluids* **73**, 172–203.

ZHANG, A.M., CUI, P., CUI, J. & WANG, Q.X. 2015 Experimental study on bubble dynamics subject to buoyancy. *J. Fluid Mech.* **776**, 137–160.

ZHANG, J.-Y., DU, Y.-X., LIU, J.-Q., SUN, Y.-R., YAO, Z.-F. & ZHONG, Q. 2022 Experimental and numerical investigations of the collapse of a laser-induced cavitation bubble near a solid wall. *J. Hydrodyn.* **34** (2), 189–199.

ZHANG, Y., XIE, X., ZHANG, Y. & DU, X. 2019 Experimental study of influences of a particle on the collapsing dynamics of a laser-induced cavitation bubble near a solid wall. *Exp. Therm. Fluid Sci.* **105**, 289–306.

https://doi.org/10.1017/jfm.2026.11781 Published online by Cambridge University Press

ZHAO, B. & COUTIER-DELGOSHA, O. 2023 The impacts of material acoustic impedance and thickness on single laser-induced bubble dynamics and determining factors in resulting pressure. *Phys. Fluids* **35** (10), 103303.

ZHAO, X., MA, W., CHEN, J., XIANG, G., ZHONG, P. & WANG, K. 2024 Vapour bubbles produced by long-pulsed laser: a race between advection and phase transition. *J. Fluid Mech.* **999**, A103.

ZHAO, X., MA, W., ISLAM, S., NARKHEDE, A. & WANG, K. 2026 M2C: An open-source software for multiphysics simulation of compressible multi-material flows and fluid-structure interactions. *Comput. Phys. Commun.* **321**, 110023.

ZHAO, X., MA, W. & WANG, K. 2023 Simulating laser-fluid coupling and laser-induced cavitation using embedded boundary and level set methods. *J. Comput. Phys.* **472**, 111656.

ZWAAN, E., LE GAC, S., TSUJI, K. & OHL, C.-D. 2007 Controlled cavitation in microfluidic systems. *Phys. Rev. Lett.* **98** (25), 254501.

https://doi.org/10.1017/jfm.2026.11781 Published online by Cambridge University Press